Delft University of Technology

Design and optimization for industrial reactor and crude separation process via coupling mechanistic kinetics with heat/momentum transfers

Acetic acid hydrogenation to ethanol

Zhou, Can; You, Chen Xi; Liu, Yang; Shi, Hui; Cui, Chengtian; Tang, Jihai; Cui, Mifen; Qiao, Xu; Xia, Ming

DOI
10.1016/j.ijhydene.2025.04.209

Publication date
2025

Document Version
Final published version

Published in
International Journal of Hydrogen Energy

Citation (APA)
Zhou, C., You, C. X., Liu, Y., Shi, H., Cui, C., Tang, J., Cui, M., Qiao, X., & Xia, M. (2025). Design and optimization for industrial reactor and crude separation process via coupling mechanistic kinetics with heat/momentum transfers: Acetic acid hydrogenation to ethanol. *International Journal of Hydrogen Energy*, *130*, 462-479. https://doi.org/10.1016/j.ijhydene.2025.04.209

International Journal of Hydrogen Energy 130 (2025) 462–479

Contents lists available at ScienceDirect

International Journal of Hydrogen Energy

journal homepage: www.elsevier.com/locate/he

Design and optimization for industrial reactor and crude separation process via coupling mechanistic kinetics with heat/momentum transfers: Acetic acid hydrogenation to ethanol

Can Zhou [a], Chen-Xi You [a], Yang Liu [a], Hui Shi [b], Chengtian Cui [d,e], Jihai Tang [a,c], Mifen Cui [a], Xu Qiao [a,c], Ming Xia [a,*]

[a] *State Key Laboratory of Materials-Oriented Chemical Engineering, College of Chemical Engineering, Nanjing Tech University, Nanjing, 211816, PR China*
[b] *School of Chemistry and Molecular Engineering, Nanjing Tech University, Nanjing, 211816, PR China*
[c] *Jiangsu National Synergetic Innovation Center for Advanced Materials (SICAM), Nanjing, 211800, PR China*
[d] *Department of Chemical Engineering, Delft University of Technology, Van der Maasweg 9, 2629 HZ, Delft, the Netherlands*
[e] *Process and Systems Engineering Laboratory, Faculty of Science and Engineering, Åbo Akademi University, Henrikinkatu 2, FI-20500, Turku, Finland*

ARTICLE INFO

Keywords:
Acetic acid
Hydrogenation
Ethanol
Multi-tubular fixed-bed reactor
N-Methyl-2-pyrrolidone

ABSTRACT

Ethanol is used to produce various value-added chemicals and as automobile fuel. Acetic acid hydrogenation to ethanol is of practical significance to meet the increasing market. However, limited engineering research for reactor and crude separation process for the acetic acid hydrogenation to ethanol despite the increasingly mature catalyst system. Moreover, the traditional approach of industrial reactor design mainly relies on point data and inadequately quantifies the strong coupling between reaction rate and transfers within the reactor, which is prone to local and loose design and optimization. In this work, a coupled design approach that combines kinetics with transfers is proposed for designing and optimizing the multi-tubular fixed-bed reactor for the acetic acid hydrogenation to ethanol. To efficiently achieve the products crude separation, staged cooling/flash/absorption/desorption units featuring with N-methyl-2-pyrrolidone as an absorbent is proposed, numerically designed and optimized. Further heuristic heat integration is also investigated to conserve extra energy of the preliminary process, which features that a by-product steam generated from ethanol synthesis reactor is utilized to drive the reboiler of the desorption. It is demonstrated that the heat-integrated process presents significant economic and emission advantages compared with the preliminary process, specifically with 36.5 % and 10.9 % reductions in operating cost and total annual cost respectively, as well as 58.1 % reductions in CO_2 emissions. The cost of synthesizing ethanol with 100 ktpy production is as low as 14.25 $/t. This work could provide a feasible and promising reactor and crude separation process for acetic acid hydrogenation to ethanol, which features economic, high-efficient, energy-saving, and low-carbon.

1. Introduction

In recent years, ethanol (EtOH), which can be used as automobile fuel alone or mixed with gasoline, has received widespread attention as an alternative to petroleum-derived fuels [1]. Besides, ethanol can also be used to produce various value-added chemicals [2,3]. Unlike the traditional processes to produce ethanol, such as ethylene hydration and fermentation [4], acetic acid (AcOH) hydrogenation to ethanol is a short process with relatively mild conditions, and high conversion and selectivity. The energy structure of China is rich in coal, poor in oil, and low in gas in China, which promotes the maturity of methanol carbonylation that enables excessive production of inexpensive acetic acid from coal [5,6]. Thus, converting acetic acid to ethanol is of significant strategic and practical significance perspective.

The catalyst system for acetic acid hydrogenation to ethanol has become greatly mature. Noble metal catalysts such as Pt [7,8], Pd [9], Ru [10,11], and Rh [12], and non-noble metal catalysts such as Ni [13] and Cu [14,15], have been studied for acetic acid hydrogenation to ethanol process in the past decades. However, relevant processes and engineering research that match the catalyst system are not found. This may hinder the application and development of technology for acetic acid hydrogenation to ethanol.

---

* Corresponding author.
E-mail addresses: Sciengart@163.com, mxia@njtech.edu.cn (M. Xia).

https://doi.org/10.1016/j.ijhydene.2025.04.209
Received 31 December 2024; Received in revised form 19 March 2025; Accepted 11 April 2025

Kinetics and thermodynamics are necessary for process studies. Although some scholars have studied reaction kinetics to provide the basis for designing reactors [16–19], the kinetics cannot be directly applied to reactors in simulation and study. The kinetics must be fitted and converted for simulation using software such as Aspen Plus. In addition, published vapor-liquid equilibrium data provide a thermodynamic basis for separation [20,21]. Therefore, we investigate the reactor and separation of acetic acid hydrogenation to ethanol based on existing kinetics and thermodynamics.

In the design of industrial reactors such as fixed-bed for hydrogenation reactions, the traditional approach of obtaining the preferred space-time yield (STY) and operating parameters of reactors depends on point data from single-tube experiments. In this way, the catalyst loading (M_{cat}) can be calculated from STY and production. Then, standard tube diameter and length are selected for arrangement in reactors and compared for volume, resulting in optimum structural parameters. However, this approach fails to perform global optimization and design of reactors due to relying on point data. Both structural parameters and operating parameters all affect heat transfer coefficient and pressure drop (ΔP) and then influence reactions. These coupling factors often cannot be considered if point data from single-tube experiments is used directly. Globally design and optimization of reactors can not only obtain maximum production based on optimum parameters but also avoid issues with thermal stability and momentum transfer. Thus, researching the coupling between the reaction rate and transfers of heat and momentum is crucial for designing and optimizing reactors. In this work, we propose a coupled design approach that combines kinetics with transfers and use it to design and optimize the reactor for ethanol.

In the separation of reaction system with hydrogen (H_2), cryogenic separation often suffers from high operating cost [22]. In contrast, physical absorption has the advantages of easy operation, high selectivity, and low cost, which is widely used for separating mixed gas. Particularly, the choice of absorbent is critical for absorption, as it directly determines the efficiency and economy of the absorption process. Ethylene Glycol (EG) and Glycerol (Gly) have been mainly used to absorb ethanol [23,24]. In this process, ethyl acetate (EtOAc) as the byproduct also needs to be recovered, but EG and Gly as absorbents are unable to meet the requirement of separation. In this work, A new absorbent is selected to recover both ethanol and ethyl acetate and compared with EG and Gly in some aspects. In addition, we design and provide a crude separation process including absorption and desorption, and then it is optimized by single-factor methods.

This work proposes a novel energy-saving reaction-crude separation process for acetic acid hydrogenation to ethanol, including reaction and crude separation section. Firstly, the reaction kinetics are converted, and the thermodynamic model with the regressed binary interaction parameters is studied to investigate the entire process. The industrial reactor for synthesizing ethanol is designed and optimized based on the coupled design approach. Then the crude separation process with a new absorbent for recovering ethanol, including absorption and desorption, is modeled and optimized. Finally, the proposed process is evaluated and optimized from the view of energy.

2. Process studied

2.1. Reaction kinetics

The reaction kinetics of acetic acid hydrogenation to ethanol over the $PtSn/K/Al_2O_3$ catalyst are given by Zhou et al. [25], considering two main reactions (R1: acetic acid hydrogenation and R2: esterification) as follows:

$$\begin{gathered} R1: CH_3COOH + 2H_2 \rightarrow C_2H_5OH + H_2O \\ \Delta_r H_m^\theta = -44.17\ kJ/mol \end{gathered} \tag{1}$$

$$\begin{gathered} R2: CH_3COOH + C_2H_5OH \rightarrow CH_3COOC_2H_5 + H_2O \\ \Delta_r H_m^\theta = -18.37\ kJ/mol \end{gathered} \tag{2}$$

In this work, the influence of catalyst particle size on efficiency of particles is not considered. Since the STY of ethanol from the single-tube pilot experiment using a large particle catalyst is comparable to those calculated by the present kinetics, and this paper focuses on the conceptual design of the reaction process, the reaction kinetics are still used in this paper for the subsequent modeling and simulation.

The kinetics are described by Langmuir-Hinshelwood-Hougen-Watson (LHHW) equations. The LHHW kinetic structure mainly consists of three terms: kinetic term, driving-force term, and adsorption term [26]. It is important to convert the reaction rate equations and their units in the original paper into the form required by Aspen Plus as a basis for reactor simulation and optimization. The original data is pressures in MPa and reaction rates in $mol \cdot h^{-1} \cdot g_{cat}^{-1}$. These must be transformed to use Pascals and $mol \cdot s^{-1} \cdot g_{cat}^{-1}$. The final reaction rates of acetic acid consumption for hydrogenation and esterification are converted and represented by Eq. (3), with each specific term listed in Table 1. Table S1 gives the kinetic and adsorption parameters input into the Aspen LHHW reaction model to implement these kinetics.

Table 1
Driving-force term and adsorption term of R1 and R2.

$R_{AcOH,1}$	
Driving-force term	
Term1 ($mol \cdot Pa^2/s/g_{cat}$)	$1.678 \times 10^{-8} \times \exp\left(\frac{-4276.16}{T}\right) P_{H_2}^2 P_{AcOH}$
Term2 ($mol \cdot Pa^2/s/g_{cat}$)	$1.7 \times 10^{-3} \times \exp\left(\frac{-8842.16}{T} - 26.49 + 6.011 \times lnT - 4.308 \times 10^{-3} \times T\right) P_{EtOH} P_{H_2O}$
Adsorption term	
Term3 (Pa)	$(P_{H_2O} P_{H_2})^{0.5}$
Term4 (Pa)	$3.927 \times 10^{-9} \times \exp\left(\frac{3449.6}{T}\right) P_{AcOH} (P_{H_2O} P_{H_2})^{0.5}$
Term5 (Pa)	$9.33 \times 10^{-4} \times \exp\left(\frac{-1868.17}{T}\right) P_{H_2} {P_{H_2O}}^{0.5}$
Term6 (Pa)	$2.52 \times 10^{-9} \times \exp\left(\frac{330.77}{T}\right) P_{EtOAc} (P_{H_2O} P_{H_2})^{0.5}$
Term7 (Pa)	$9.75 \times 10^{-4} \times \exp\left(\frac{1293.84}{T}\right) P_{EtOH} {P_{H_2O}}^{0.5}$
Term8 (Pa)	$8.553 \times 10^{-4} \times \exp\left(\frac{-1019.85}{T}\right) P_{AcOH} P_{H_2} {P_{H_2O}}^{-0.5}$
Term9 (Pa)	$1.059 \times 10^{-5} \times \exp\left(\frac{-160.21}{T}\right) {P_{H_2O}}^{1.5}$
$R_{AcOH,2}$	
Driving-force term	
Term1 ($mol \cdot Pa/s/g_{cat}$)	$9.736 \times 10^{-8} \times \exp\left(\frac{-3537.17}{T}\right) P_{AcOH} P_{EtOH}$
Term2 ($mol \cdot Pa/s/g_{cat}$)	$9.736 \times 10^{-8} \times \exp\left(\frac{-6165.17}{T} + 16.56 - 2.353 \times lnT + 2.11 \times 10^{-3} \times T\right) P_{EtOAc} P_{H_2O}$
Adsorption term	
Term3 ($Pa^{0.5}$)	$P_{H_2O}^{0.5}$
Term4 ($Pa^{0.5}$)	$3.927 \times 10^{-9} \times \exp\left(\frac{3449.6}{T}\right) P_{AcOH} P_{H_2O}^{0.5}$
Term5 ($Pa^{0.5}$)	$9.33 \times 10^{-4} \times \exp\left(\frac{-1868.17}{T}\right) (P_{H_2} P_{H_2O})^{0.5}$
Term6 ($Pa^{0.5}$)	$2.52 \times 10^{-9} \times \exp\left(\frac{330.77}{T}\right) P_{EtOAc} {P_{H_2O}}^{0.5}$
Term7 ($Pa^{0.5}$)	$9.75 \times 10^{-4} \times \exp\left(\frac{1293.84}{T}\right) P_{EtOH} {P_{H_2O}}^{0.5} {P_{H_2}}^{-0.5}$
Term8 ($Pa^{0.5}$)	$8.553 \times 10^{-4} \times \exp\left(\frac{-1019.85}{T}\right) P_{AcOH} {P_{H_2}}^{0.5} {P_{H_2O}}^{-0.5}$
Term9 ($Pa^{0.5}$)	$1.059 \times 10^{-5} \times \exp\left(\frac{-160.21}{T}\right) {P_{H_2O}}^{1.5} {P_{H_2}}^{-0.5}$

$$R_{AcOH} = (kinetic\ term)\frac{(driving - force\ term)}{adsorption\ term} = \frac{term1 - term2}{(term3 + term4 + term5 + term6 + term7 + term8 + term9)^2} \quad (3)$$

The reactor is simulated and the reaction kinetics are validated in Aspen Plus by using the RPlug model. Fig. 1a, b, and c show the match of experimental and simulated values of acetic acid conversion and ethanol selectivity at different pressures, temperatures, and weight hourly space velocity (WHSV) of acetic acid, respectively. The regular curves for simulated values of conversion and selectivity are basically in agreement with experimental values, indicating that the converted kinetic model can accurately describe the process of acetic acid hydrogenation reaction, which can be used for reactor process simulation and optimization.

2.2. Thermodynamic property method

The thermodynamic method is key to accurately simulating the subsequent separation process. Considering the system containing acetic acid and ethanol that are susceptible to vapor-phase association [27], the NRTL-HOC model can be well used to describe the vapor-liquid phase equilibrium relationship [28,29], in which the NRTL model describes the non-ideal state of the liquid phase, the Hayden-O'Connell equation [30] describes the non-ideal state of the vapor phase, and the hydrogen (H_2) is considered as Henry's component.

In this work, we retrieved and selected several alternative potential absorbents including EG, Gly, and N-methyl-2-pyrrolidone (NMP) [31] from previous literature. The binary interaction parameters for EG and Gly as absorbents are given in Table S2 and Table S3 and the binary interaction parameters for NMP as absorbent are given below.

Binary interaction parameters of AcOH-NMP and EtOAc-NMP are missing in Aspen Plus. Regression of binary interaction parameters of the model by fitting vapor-liquid equilibrium (VLE) data from the literature. The binary interaction parameters between the remaining components were used as inbuilt values and the binary interaction parameters between components are shown in Table 2. The VLE data for AcOH-NMP were obtained from Chang et al. [20], and for EtOAc-NMP from Yang et al. [21].

Fig. 2a and b represent the T-x-y curves of AcOH-NMP and EtOAc-NMP, respectively. It can be observed that the calculated VLE curves are in good agreement with the experimental values, indicating that the NRTL-HOC model can accurately describe the VLE of the system and can be used for process simulation.

3. Process design and optimization

Fig. 3 shows a conceptual block flowsheet diagram of the design of the reaction-crude separation process for acetic acid hydrogenation to ethanol. The reaction-crude separation process mainly consists of two parts: reaction and crude separation by absorption. Acetic acid and

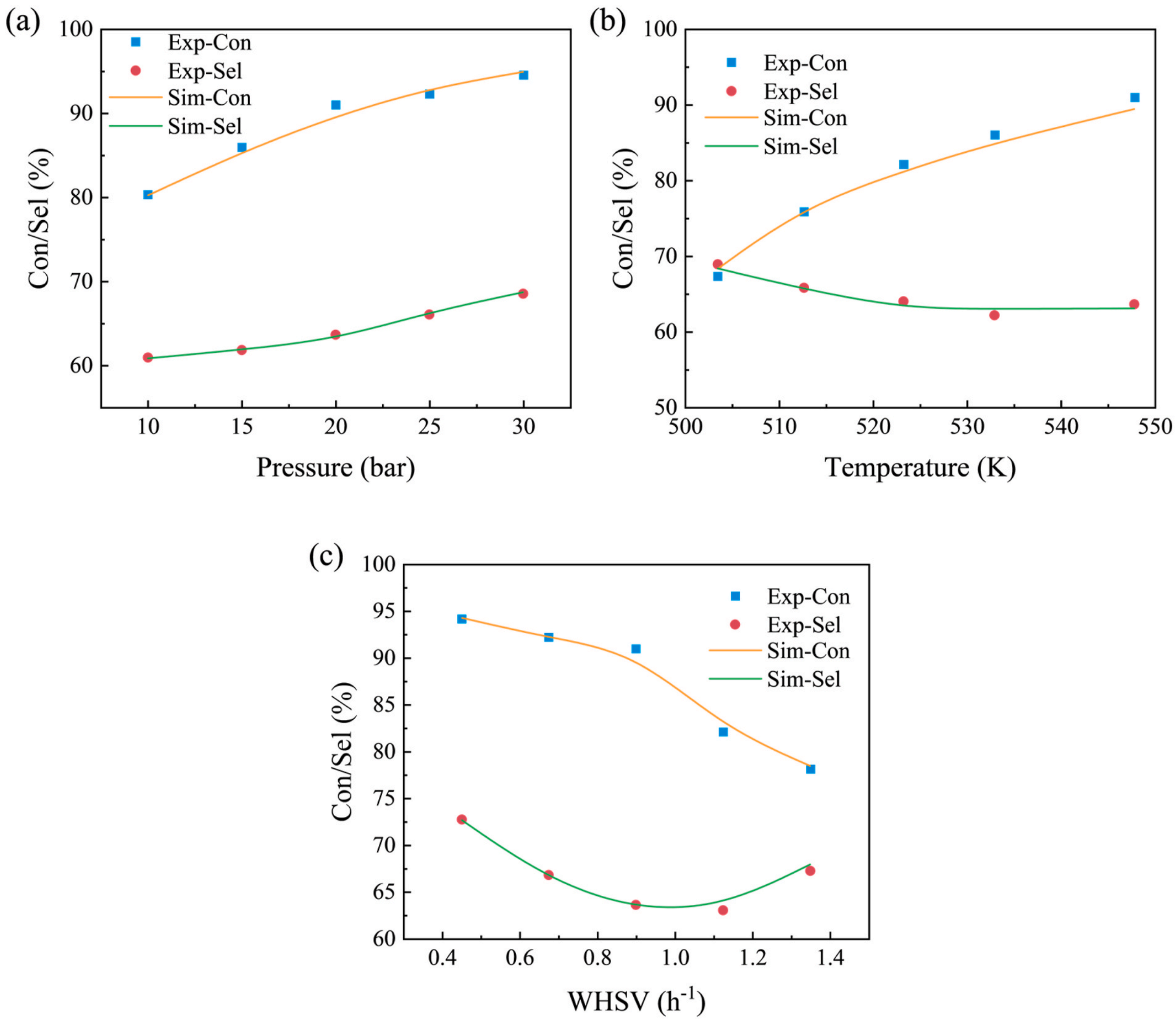

Fig. 1. Experimental and simulated values of AcOH Conversion and EtOH Selectivity at different (a) pressures, (b) temperatures, and (c) WHSVs.

Table 2
Binary interaction parameters of the NRTL-HOC model.[a].

Component i	EtOH	EtOH	Water	Water	AcOH	AcOH	AcOH	EtOH	AcOH	EtOAc
Component j	Water	EtOAc	EtOAc	NMP	EtOH	Water	EtOAc	NMP	NMP	NMP
Aij	−0.801	−1.151	9.463	7.408	0	−1.976	0	2.146	0	1.554
Aji	3.458	−0.243	−3.720	−2.244	0	3.329	0	−1.749	0	0.909
bij (K)	246.18	524.424	−1705.68	−2279.96	−252.482	609.889	−235.279	−482.196	187.075	−991.073
bji (K)	−586.081	282.956	1286.138	533.847	225.476	−723.888	515.821	254.607	−670.872	560.815
cij	0.3	0.3	0.2	0.3	0.3	0.3	0.3	0.5	0.3	0.3

[a] Selecting the NRTL-HOC property method to regress the binary interaction parameters of AcOH-NMP, selecting the NRTL property method to regress the binary interaction parameters of EtOAc-NMP.

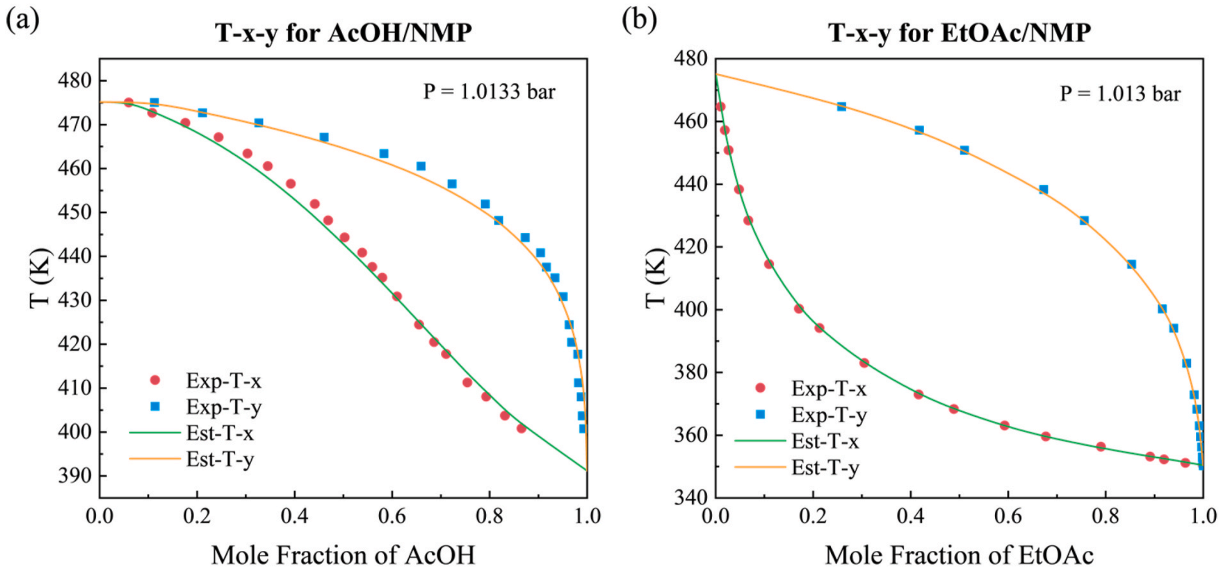

Fig. 2. (a) AcOH-NMP T-x-y curves at 1.0133 bar, (b) EtOAc-NMP T-x-y curves at 1.013 bar.

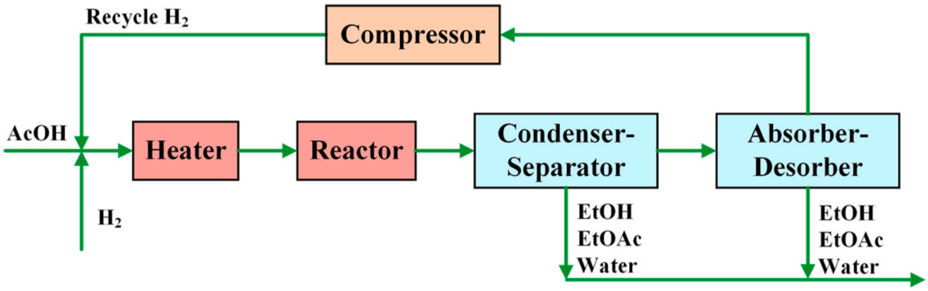

Fig. 3. Conceptual block flowsheet diagram of the reaction-crude separation process.

hydrogen are mixed and passed through a heater and into the reactor for reaction. The reactor effluent mainly containing acetic acid, hydrogen, ethanol, ethyl acetate, and water obtained from the reaction was cooled and then separated by the vapor-liquid separator, which ethanol, ethyl acetate, and water were mainly separated. The hydrogen with a small amount of ethanol is got into the absorber. Finally, the high-purity hydrogen is recycled back to the reactor through a compressor, and the ethanol is completely recovered.

3.1. Reactor design and optimization

For the design of industrial reactors, acetic acid hydrogenation is an exothermic reaction with a large enthalpy change and the enthalpy change of esterification is moderate [32]. Therefore, when the reaction rate and ethanol selectivity are large, a large amount of heat is released during production and the exothermic rate is also large. Also considering the relatively high sensitivity of ethanol selectivity to reaction temperature, conventional fixed-bed reactors such as packed-bed reactors may not meet the heat transfer requirement. This type of reactor could cause an uneven axial/radial bed temperature profile, high axial hot spot, and thus deteriorative ethanol selectivity. Moreover, serious problems such as catalyst sintering and reactor damaging are prone to occur. Multi-tubular fixed-bed reactors [33,34] commonly offer a large ratio of heat transfer area to volume, which ensures sufficient heat removal rate to deal with the generated reaction heat rate within the reactor and are widely used in hydrogenation reactions with large thermal effects [35,36]. In addition, saturated water is used to control the temperature profile of the reactor to ensure safe operation at the optimum reaction temperature and to avoid thermal runaway [37,38]. Therefore, in this paper, a multi-tubular fixed-bed reactor is developed for acetic acid hydrogenation to ethanol from reaction kinetics, coupled with heat and momentum transfers.

3.1.1. Design and optimization method

Reactor design and optimization are at the heart of the actual project design and even directly affect the economics of the entire technology. In the case of a multi-tubular fixed-bed reactor, M_{cat} directly determines the volume of the bed (V_b) when the catalyst particle characteristics and filling method are determined. However, the design of a multi-tubular fixed-bed reactor is to determine the volume of the reactor (V_r), which involves several structural parameters such as bed height (L), tube diameter, and number of tubes (N_t). In addition, more favorable operating parameters not only increase the reaction rate and production but also enhance the safety and stability of the reactor.

The conventional design of a multi-tubular fixed-bed reactor is primarily based on single-tube experimental point data. It was assumed that the operating parameters of each tube in the industrial reactor were the same as those of the single-tube experiment, and M_{cat} was calculated based on the STY of the single tube and the target production. Further, the industrial reactor was designed and the reactor structural parameters and V_r were obtained by standard tube diameter and length. In single-tube experiments, STY can be effectively enhanced and reaction performance optimized by appropriately increasing WHSV or reducing M_{cat}. However, this may result in poor momentum transfer and reaction inefficiency. Conversely, taking the approach of reducing WHSV or increasing M_{cat}, although the problems can be solved, tends to limit the catalyst performance to be fully utilized, thus leading to a decrease in STY. Therefore, it is time-consuming and labor-intensive to find the right WHSV and M_{cat} to maximize the reaction performance through single-tube experiments, which is not conducive to reactor design and process development.

From the heat transfer perspective, WHSV and tube diameter directly affect the temperature profile in the multi-tubular fixed-bed reactor. On the one hand, WHSV affects convective heat transfer and reaction rates within the reactor bed. On the other hand, the use of larger tube diameters for the same V_b and operating parameters is expected to reduce the V_r. However, too large tube diameter results in poorer heat transfer, and large amounts of heat generated by the reaction cannot be timely removed, and the bed may experience temperature runaway or even cause catalyst sintering. The axial temperature profile along the reactor is usually shown in Fig. 4, where the bed temperature first rises to a high point along the axial direction and then decreases and finally flattens out. The highest point of the profile is often referred to as the maximum temperature of the bed (T_{max}) or hot spot. Considering the tolerance temperature and service life of the catalyst, reaction temperature (503–558 K), adverse effects that are difficult to recover may occur at T_{max} exceeding 568.15K, which is taken as the critical T_{max}.

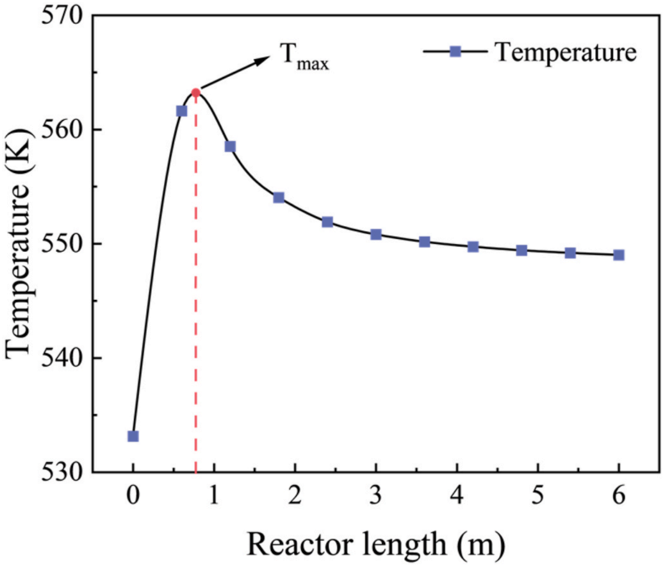

Fig. 4. Axial temperature profile along the multi-tubular fixed-bed reactor. Initial operating parameters of reactor: $d_i = 32$ mm, $L = 6$ m, WHSV = 1 h^{-1}, $M_{cat} = 25000$ kg, $U = 300$ W/m^2/K, $\Delta P = 0.6$ bar, $T_s = 548.15$ K, $P_p = 20$ bar, $M_r = 10$, $T_p = 533.15$K.

The ΔP is also a limiting factor for reactor design when analyzed from the momentum transfer perspective. Too large ΔP leads to poorer momentum transfer and higher operating costs, which are detrimental to the reaction process and stable reactor operation. ΔP is affected by both particle characteristics and WHSV, and tube diameter directly affects ΔP. Based on the previous section, it is considered that the fixed 4 mm catalyst particle size (d_s) is consistent with the STY of the pilot scale experiment, and the effect of the change in d_s on ΔP is ignored. On the one hand, increasing WHSV increases superficial gas velocity, causing ΔP to increase. On the other hand, increasing tube diameter decreases bed voidage (ε_b), causing ΔP to increase. Considering that the reactor operating pressure is in the range of 10–30 bar, 0.6 bar (3 % × 20 bar) was selected as the critical ΔP.

In summary, the relationship between heat and momentum transfer is complex. For the fixed V_b, increasing the tube diameter can significantly reduce V_r, however, increasing the tube diameter could deteriorate heat transfer and increase ΔP. It is possible to reduce ΔP by lowering WHSV, but this may also deteriorate heat transfer. To achieve the desired production, lowering WHSV will increase M_{cat} and thus V_b. Finally, V_r may instead increase. Therefore, finding appropriate WHSV and tube diameter should be significant, but using the traditional reactor design method is difficult.

For the design of a multi-tubular fixed-bed reactor, there exists an appropriate WHSV and tube diameter to minimize V_b and V_r while maintaining an appropriate temperature profile and ΔP. Therefore, this paper aims to determine M_{cat} at different STYs with target production and to study the effect of WHSV on temperature profile and ΔP based on kinetics. Then different sizes of the standard tube were selected to investigate the influence of tube diameter on temperature profile and ΔP in the bed. To this end, this paper proposes a two-factor (WHSV and tube diameter) influenced multi-tubular fixed-bed reactor design and optimization method through process simulation and numerical calculations, combined with the heat and momentum transfer model.

Fig. 5 shows a conceptual block flowsheet diagram of the multi-tubular fixed-bed reactor for acetic acid hydrogenation to ethanol, the two-factor optimization sequence of the multi-tubular fixed-bed reactor design, and the single-factor (operating parameters) optimization sequence of the multi-tubular fixed-bed reactor. For reactors with small reaction heat or small tube diameters, the radial temperature profile is even. This paper focuses on the relationship between tube diameter and axial temperature profile in the bed, it may be convenient to use a one-dimensional model that considers only axial gradients of temperature [39,40].

The overall heat transfer coefficient (U) between the bed and saturated water is given by Eq. (4).

$$\frac{1}{U}=\frac{1}{\alpha_b}+\frac{1}{\alpha_f}+\frac{\delta}{\lambda_s}+R_c \tag{4}$$

Where α_b is the convective heat transfer coefficient from the bed to the tube wall, W/m^2/K. α_f is the convective heat transfer coefficient of saturated water outside the tube to the tube wall, W/m^2/K. λ_s is the thermal conductivity of the tube wall, W/m/K. δ is the tube wall thickness, m. R_c is the fouling coefficient of the bed as well as outside of the tube, $m^2 \cdot$K/W. Table S4 gives the expansion of each term in the equation.

The ΔP of the bed is given by Ergun's equation [41].

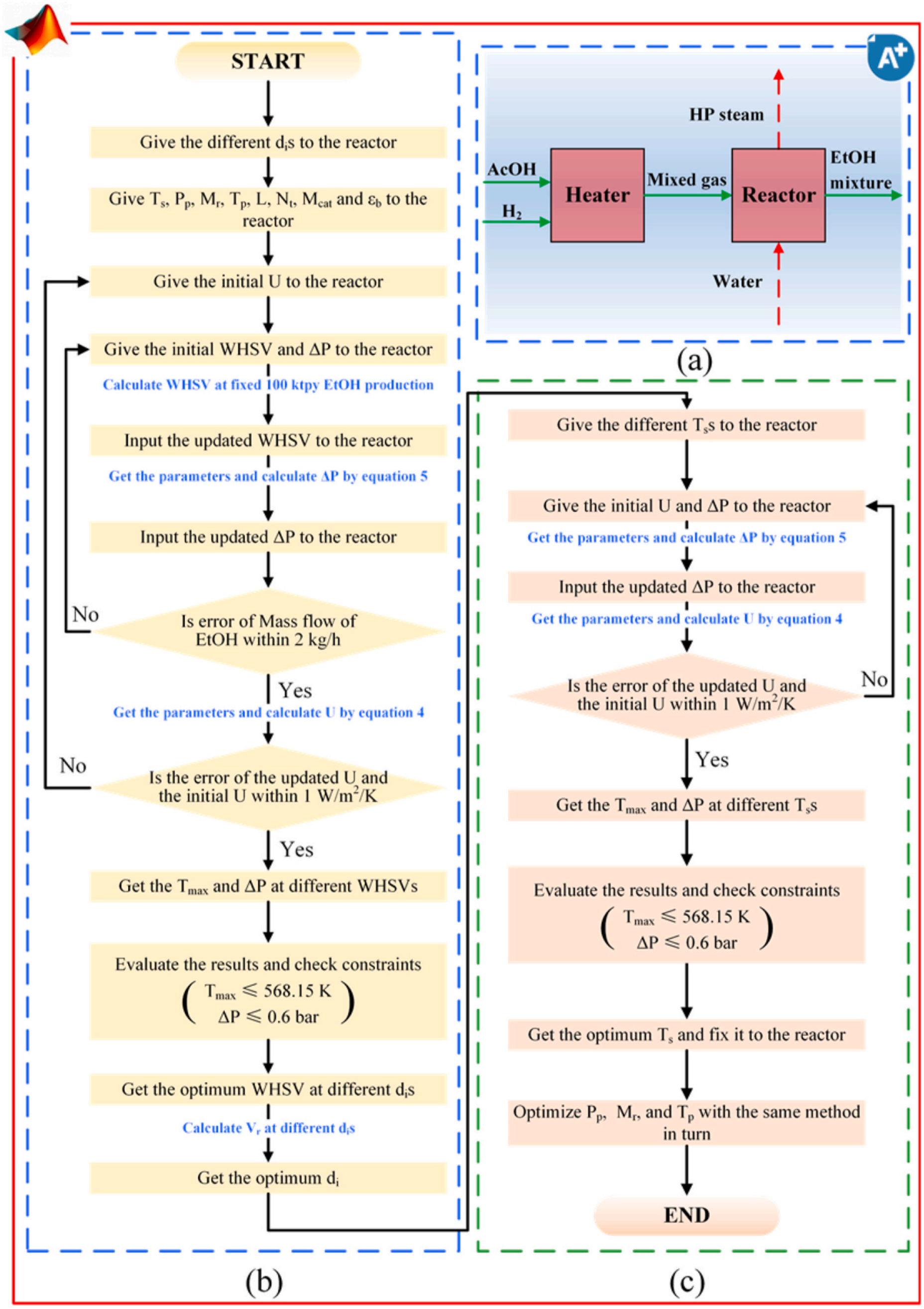

Fig. 5. (a) Conceptual block flowsheet diagram of the multi-tubular fixed-bed reactor, (b) Two-factor optimization sequence of the multi-tubular fixed-bed reactor design, (c) Single-factor optimization sequence of the multi-tubular fixed-bed reactor.

$$\Delta P = \frac{f' \times \rho \times u_m^2 \times L \times (1-\varepsilon_b)}{d_s \times \varepsilon_b^3} \tag{5}$$

$$f' = 1.75 + \frac{150}{Re_M} \tag{6}$$

$$Re_M = \frac{d_s \times \rho \times u_m}{\mu \times (1-\varepsilon_b)} \tag{7}$$

Where f' is the coefficient of frictional resistance. ρ is the density of the gas, kg/m^3. u_m is superficial gas velocity, m/s. L is bed height, m. ε_b is bed voidage. d_s is catalyst particle size, m. Re_M is the corrected Reynolds number. μ is gas viscosity, kg/m/s.

During the design and optimization of the reactor, the inner diameter of the tube (d_i) was selected as 19 mm, 26 mm, 32 mm, 38 mm, and 50 mm. To better study the effect of tube diameter on temperature profile and ΔP of the multi-tubular fixed-bed reactor, L was selected as 6 m. In addition, this paper considers the effect of changing tube diameter on ε_b, but as ε_b has less effect on the bed density, the relationship between tube diameter and ε_b is shown in Table S5. Therefore, the estimated bed density of 1000 kg/m^3 was selected at the fixed d_s. The M_{cat} and V_b of different STYs at 100 kilotons per year (ktpy) ethanol are shown in Table 3.

Although mechanistic kinetic is used for the reactor model, it coupled heat and momentum transfer to form macroscopic kinetics. Moreover, the reactor is designed and optimized within the range of experimental conditions from the kinetics. Therefore, the reactor can be accurately modeled in this paper. Aspen Plus V12 software was used to construct the reactor model and the design and optimization of the reactor involved establishing a connection between MATLAB 2019A and

Table 3
The M_{cat} and V_b of different STYs at 100 ktpy EtOH.

STY (g/(g_{cat}·h))	0.25	0.3	0.35	0.4	0.45	0.5	0.55
M_{cat} (kg)	50000	41666.7	35714.3	31250	27777.8	25000	22727.3
V_b (m^3)	50.00	41.67	35.71	31.25	27.78	25.00	22.73

Aspen Plus V12 software. The connection between MATLAB 2019A and Aspen Plus V12 can greatly reduce the time required to run Aspen Plus V12 alone and work with data. **S1** gives how to connect Aspen Plus to MATLAB 2019A. MATLAB 2019A and Aspen Plus V12 are connected through a COM server [42]. After both establish a connection, MATLAB 2019A reads node parameters in Aspen Plus V12, which accepts values of variables, performs simulation, and passes simulation results back to MATLAB 2019A for further processing and optimization, forming an iterative structure.

Fig. 5b represents the two-factor optimization sequence of the multi-tubular fixed-bed reactor design, which is achieved by iterative calculations to determine tube diameter and WHSV. Initial reactor processes were fixed with the temperature of saturated water (T_s), the pressure of the process stream (P_p), the mole ratio of hydrogen to acetic acid (M_r), the temperature of the process stream (T_p), L, N_t, M_{cat}, and ε_b, and established at different tube diameters. U is given initial value, and WHSV and ΔP are also given initial values. We iteratively calculate WHSV at the target production and then input the updated WHSV to the reactor. We get parameters such as density and viscosity from the simulation results and get the updated ΔP by eq. (5). Now, we input the updated WHSV and ΔP and calculate whether the ethanol production differs from the target production by 2 kg/h. The updated WHSV and ΔP go to the outer iteration if the error is met. If the error is exceeded, the updated WHSV and ΔP are iteratively calculated again as initial values.

When the inner iteration is finished, the outer iteration is started. We input the updated WHSV and ΔP to the reactor, and parameters such as thermal conductivity, viscosity, and amount of heat transfer are obtained from simulation results. We get the updated U by eq. (4) and check the error between the updated U and the initial U is less than 1 W/m^2/K. The end of iteration is implemented when the error is satisfied. If it does not conform, the updated U is returned to start as the initial value.

The T_{max} and ΔP at different WHSVs are obtained through iterative calculations, and V_b is used as the optimization objective to determine the optimum WHSV under constraints. The above optimization process was repeated for different tube diameters. Finally, the optimum tube diameter was determined by calculating V_r based on the V_b of different tube diameters.

After completing the reactor design, different operating parameters were sequentially optimized. The operating parameters include T_s, P_p, M_r, and T_p. The single-factor optimization sequence considers only the effect of operating parameters on T_{max} and ΔP, which is shown in Fig. 5c. We give the initial U and ΔP to the reactor and calculate ΔP by eq. (5). Then, we get the updated ΔP and input to the reactor. Similarly, we get the updated U by eq. (4) and check the error between the updated U and the initial U is less than 1 W/m^2/K. We end the iteration when the error is satisfied. If it does not conform, the updated U is returned to the start as the initial value.

The T_{max} and ΔP were obtained by iterative calculations at different operating parameters. The STY of ethanol was used as the optimization objective. With the constraints, the operating parameters are determined.

3.1.2. Optimum structure parameters

After iterative calculations, Table 4 and Fig. 6 are obtained. Table 4 gives α_b, α_f, and U for different WHSVs at each tube diameters. Horizontally, when the tube diameter is large, α_b is less than α_f, and the convective heat transfer within the bed dominates over the overall heat transfer process. Dynamically, as the tube diameter decreases, the mass flow of gas per unit cross-sectional area increases, which increases α_b. The α_f decreases due to the increase in heat transfer area. As the tube diameter decreases below a certain value, convective heat transfer within the bed gradually ceases to dominate. Longitudinally, large WHSV corresponds to large STY in Table 4, large STY corresponds to small M_{cat} in Table 3, the reduction in M_{cat} causes the reduction in V_b, and N_t decreases due to the reduction in V_b. Increasing mass flow of gas per unit cross-sectional area increases α_b, decreasing heat transfer area increases α_f, and U increases.

The effect of different WHSVs and tube diameters on T_{max} and ΔP are analyzed in Fig. 6. From Fig. 6a, T_{max} decreases with increasing WHSV.

Table 4
Convective heat transfer coefficient within the bed and outside the tube and the overall heat transfer coefficient at different tube diameters.[a].

STY g/(g_{cat}·h)	WHSV h^{-1}	d_i = 50 mm			WHSV h^{-1}	d_i = 38 mm			WHSV h^{-1}	d_i = 32 mm		
		α_b W/m^2/K	α_f W/m^2/K	U W/m^2/K		α_b W/m^2/K	α_f W/m^2/K	U W/m^2/K		α_b W/m^2/K	α_f W/m^2/K	U W/m^2/K
0.25	0.54	375.1	1024.4	229.9	0.54	449.6	819.7	240.7	0.54	496.3	722.0	244.9
0.30	0.66	424.5	1161.5	254.7	0.67	508.9	929.4	266.6	0.67	561.9	818.6	271.3
0.35	0.79	471.8	1287.1	277.4	0.79	566.0	1030.1	290.0	0.80	624.9	907.3	295.3
0.40	0.92	517.8	1403.0	298.2	0.93	621.2	1122.8	311.5	0.93	686.1	989.0	317.2
0.4/5	1.06	562.8	1510.2	317.7	1.06	675.4	1208.6	331.3	1.07	746.1	1064.8	337.4
0.50	1.20	607.1	1609.5	335.9	1.21	728.8	1288.3	349.8	1.21	805.2	1135.1	356.2
0.55	1.34	650.9	1701.4	353.0	1.35	781.7	1362.4	367.1	1.36	863.7	1200.6	373.8

STY g/(g_{cat}·h)	WHSV h^{-1}	d_i = 26 mm			WHSV h^{-1}	d_i = 19 mm		
		α_b W/m^2/K	α_f W/m^2/K	U W/m^2/K		α_b W/m^2/K	α_f W/m^2/K	U W/m^2/K
0.25	0.55	549.1	605.4	240.5	0.55	609.5	459.0	222.1
0.30	0.67	621.7	686.4	266.7	0.67	690.2	520.4	246.7
0.35	0.80	691.5	760.8	290.3	0.80	767.8	576.8	268.9
0.40	0.93	759.3	829.4	311.8	0.93	843.2	628.8	289.1
0.45	1.07	825.8	892.9	331.6	1.07	917.1	677.0	307.7
0.50	1.21	891.4	952.1	350.0	1.22	990.0	721.9	324.8
0.55	1.36	956.4	1007.1	367.2	1.37	1062.3	763.8	340.9

[a] The δ of d_i = 50 mm is 3.5 mm, the δ of d_i = 38 mm is 3.5 mm, the δ of d_i = 32 mm is 3.0 mm, the δ of d_i = 26 mm is 3.0 mm, the δ of d_i = 19 mm is 3.0 mm. The λ_s of all tube diameters are fixed at 19 W/m/K. The R_c is fixed at 0.000526 m^2·K/W.

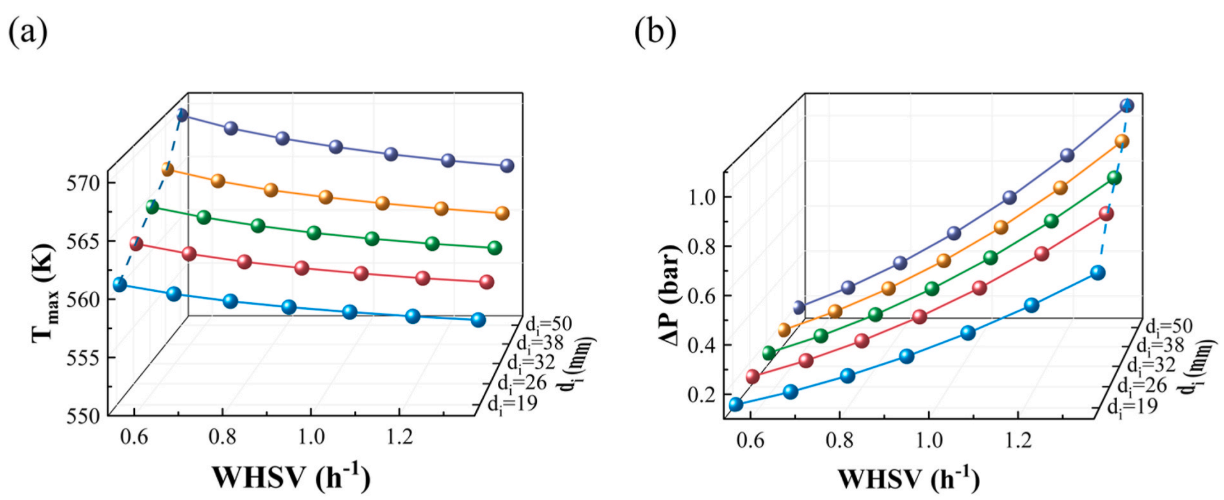

Fig. 6. The effect of WHSVs on (a) T_{max}, (b) ΔP at different tube diameters in the multi-tubular fixed-bed reactor. Operating parameters of reactor: $T_s = 548.15$ K, $P_p = 20$ bar, $M_r = 10$, $T_p = 533.15$ K.

For a certain tube diameter, increasing WHSV increases U, which decreases T_{max}. For a certain WHSV, T_{max} increases as the tube diameter increases. In addition, the effect of WHSV on T_{max} diminishes after the tube diameter is reduced. This indicates that convective heat transfer within the bed is no longer dominant.

From Fig. 6b, WHSV and tube diameter are the main factors affecting ΔP. For a certain tube diameter, increasing WHSV increases superficial gas velocity, which causes a significant increase in ΔP. When WHSV is certain, increasing tube diameter causes a decrease in ε_b and a consequent increase in ΔP. Therefore, ΔP can be effectively reduced by reducing both WHSV and tube diameter.

Based on the above analysis, the optimum WHSV for each tube diameter is determined at minimum M_{cat} and V_b, constrained by critical T_{max} and ΔP. The optimization results for the design of the multi-tubular fixed-bed reactor are shown in Table 5, which gives M_{cat} and V_b at corresponding WHSV.

Fig. 7 gives the relationship between tube diameter and V_r. At tube diameters 19, 26, and 32, heat transfer is sufficient, and WHSV is determined by pressure drop limitation. As the tube diameter increases, the bed voidage decreases and thus increases bed pressure drop. Thus, small tube diameters make pressure drop a limited factor, WHSV to be reduced to decrease pressure drop. In this case, the increase of V_b caused by pressure drop limitation is somewhat gradual. V_r reduces because of the tube diameter increasing. However, at tube diameters 38 and 45, the influence of diameter on voidage and pressure drop becomes insensitive, but heat transfer influence rises to the determinative factor. Thus, as the tube diameter increases, heat transfer limitation causes the WHSV to be reduced to decrease the generated reaction heat rate. In this case, the increase of V_b caused by heat transfer limitation is quite significant due to the highly strong nonlinearity of the reaction rate. V_r increases as the tube diameter increases. In summary, the multi-tubular fixed-bed reactor with a tube diameter of 32 mm was selected for this process study.

Table 5
Optimum WHSVs of the multi-tubular fixed-bed reactor at different tube diameters.

d_i (mm)	WHSV (h^{-1})	M_{cat} (kg)	V_b (m^3)
19	1.217	25000	25.00
26	1.070	27777.8	27.78
32	1.067	27777.8	27.78
38	0.927	31250	31.25
50	0.922	31250	31.25

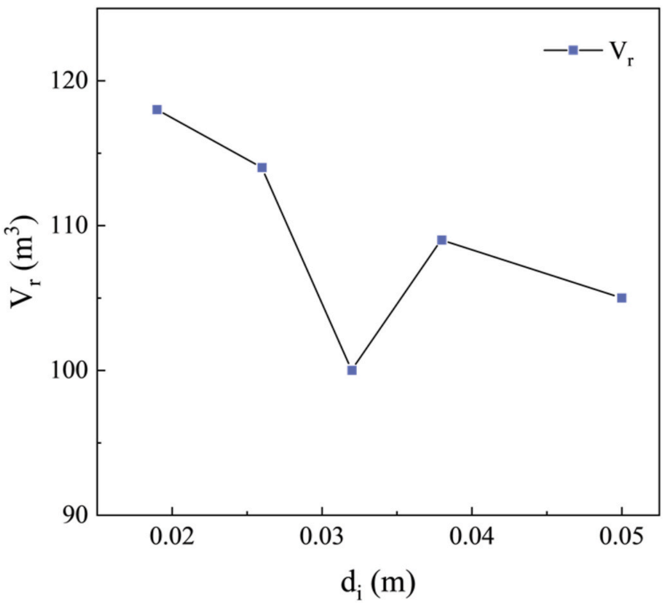

Fig. 7. The multi-tubular fixed-bed reactor volume of different tube diameters.

3.1.3. *Optimum operating parameters*

Fig. 8a, b, c, and d represent the U at different T_ss, P_ps, M_rs, and T_ps, respectively. U is negatively correlated with T_s. Whereas it is positively correlated with the other operating parameters. As T_s increases, the amount of heat transfer decreases, which weakens the convective heat transfer outside the tube, and thus reduces U. Increasing P_p or T_p increases conversion, and thus increases the amount of heat that should be removed. This will intensify convective heat transfer outside the tube and increase U. Increasing M_r increases gas volume, which increases convective heat transfer within the bed, thus increasing U.

Fig. 9a, b, c, and d show optimization results for different operating parameters, respectively. Fig. 9a represents the effect of T_s on T_{max}, ΔP, and STY. The significant increase in T_{max} shown in the figure is due to increasing T_s and decreasing U. Increasing T_s increases conversion, which causes a significant increase in STY. Moreover, the increase in conversion caused a decrease in mixture density within the bed. This causes gas velocity to increase slightly, which also causes ΔP to increase slightly.

The ΔP in Fig. 9b decreases as P_p increases. In addition to WHSV and

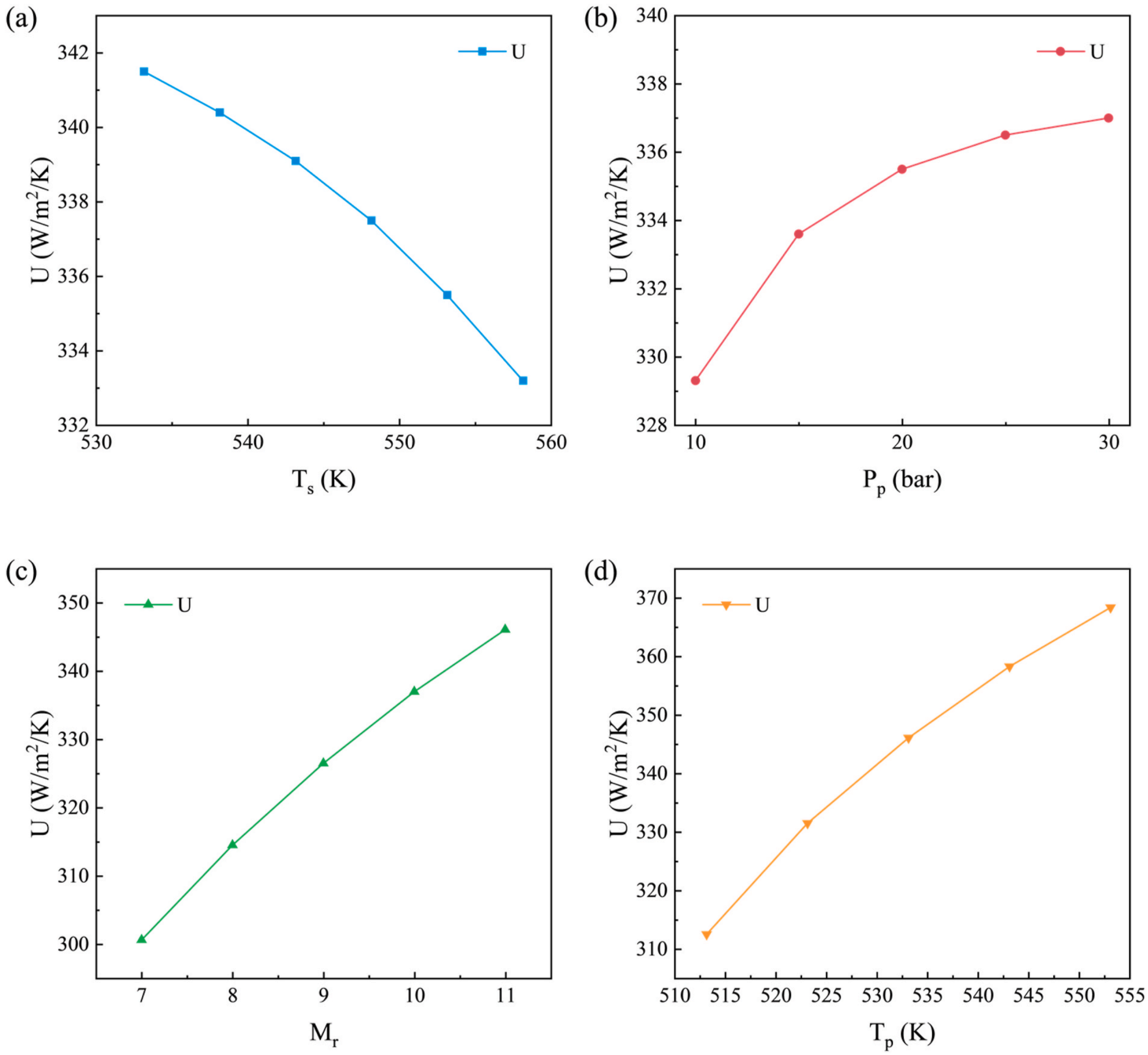

Fig. 8. (a) The U at different T_ss. Operating parameters in the reactor: $P_p = 20$ bar, $M_r = 10$, $T_p = 533.15$ K. (b) The U at different P_ps. Operating parameters in the reactor: $T_s = 553.15$ K, $M_r = 10$, $T_p = 533.15$ K. (c) The U at different M_rs. Operating parameters in the reactor: $T_s = 553.15$ K, $P_p = 30$ bar, $T_p = 533.15$ K. (d) The U at different T_ps. Operating parameters in the reactor: $T_s = 553.15$ K, $P_p = 30$ bar, $M_r = 11$.

tube diameter, pressure is also a major factor affecting ΔP. As pressure increases, gas velocity decreases, which causes a significant decrease in ΔP. Increasing pressure increases conversion, which enhances reaction exotherm. Even with a slight increase in U, T_{max} is still slightly elevated. Both STY and ΔP in Fig. 9c increase as M_r increases. Acetic acid hydrogenation is a consecutive reaction and excess hydrogen favors ethanol production [43]. Increasing M_r increases gas velocity, which causes ΔP to rise. U increases significantly, while T_{max} necessarily decreases.

It is shown that T_s, P_p, and M_r are the key operating parameters affecting performance. The T_p has little effect on the reaction [43]. It can be seen in Fig. 9d that T_p does not affect STY. Increasing U favors heat transfer. However, increasing T_p caused an increase in bed temperature, which is not conducive to the stable operation of the reactor. Therefore, preheating of the process stream is achieved by heat exchange between the inlet stream and the outlet stream of the reactor, which avoids reheating of the heater and improves reactor safety and economic efficiency. In summary, the optimum operating parameters are shown in Table 6.

3.2. *Crude separation process design and optimization*

3.2.1. *Design and optimization method*

After the reaction in the multi-tubular fixed-bed reactor, the mixture is cooled with vapor-liquid separation. The incompletely recovered ethanol and ethyl acetate are further separated and a large amount of hydrogen need to be recycled back to the reactor to participate in the reaction. Recovery of ethanol and recycling hydrogen through absorption greatly improves the economics of the process.

The ethanol mixed gas enters the absorber, and NMP acts as the absorbent to carry away ethanol and ethyl acetate in the mixture. Almost pure hydrogen separated is recycled to the reaction section as feedstock. The absorbent with solute enters the desorber to recover ethanol and ethyl acetate, and the pure absorbent survived is recycled to the absorber. The crude separation process by absorption is shown in Fig. 10. In this process, the absorber pressure is related to P_p and ΔP. To avoid excessive compression ratios of the compressor for recycling hydrogen, the pressure of the absorber at 29 bar has been determined. Due to the high bubble point (T_b) of NMP, the desorber is a low-pressure tower. This ensures operational stability and reduces the desorber's reboiler duty.

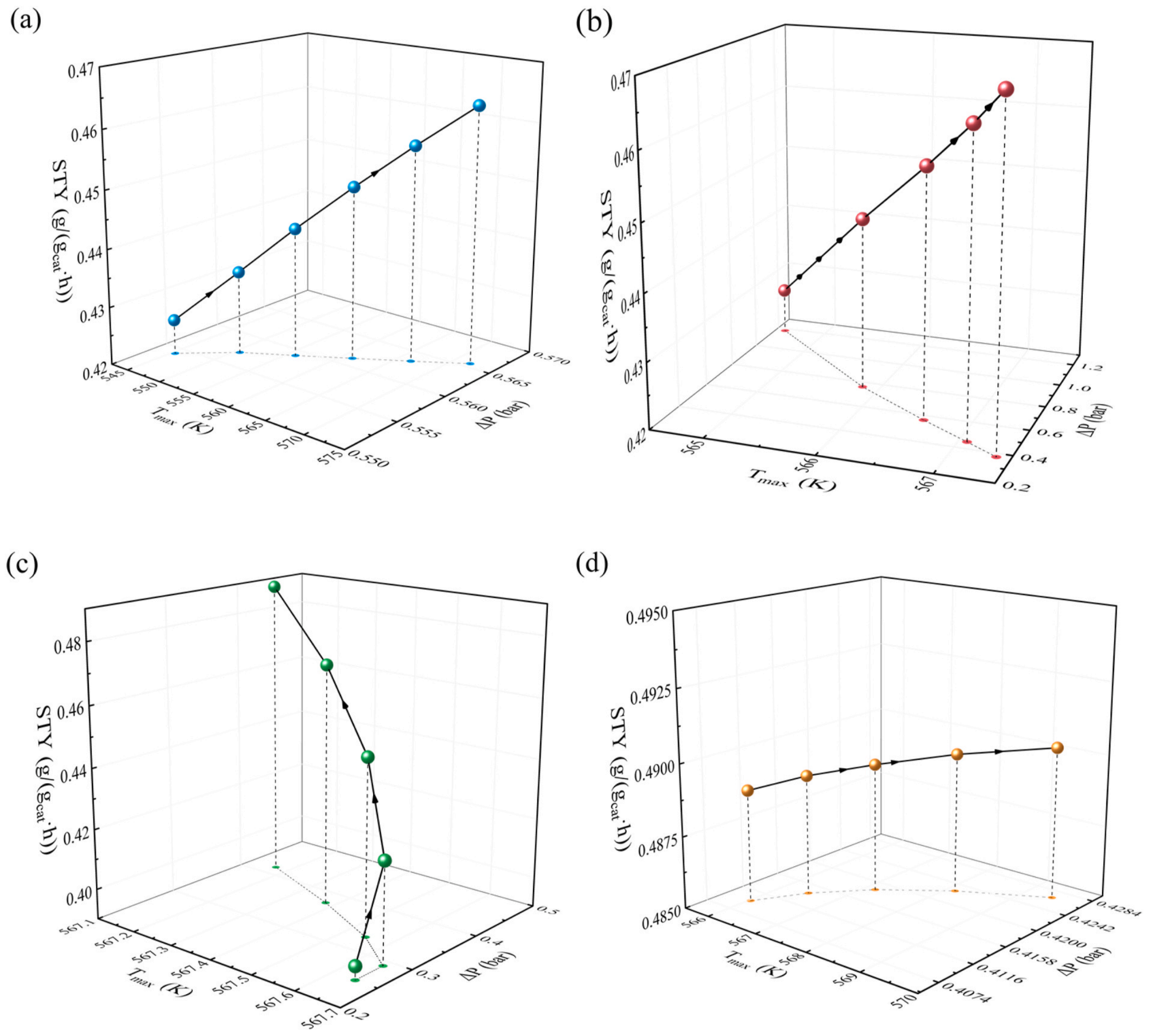

Fig. 9. The effect of (a) T_s, (b) P_p, (c) M_r, (d) T_p on T_{max}, ΔP, and STY.

Table 6

Optimum operating parameters of the multi-tubular fixed-bed reactor.

Parameters	T_s (K)	P_p (bar)	M_r	T_p (K)
Value	553.15	30	11	513.15

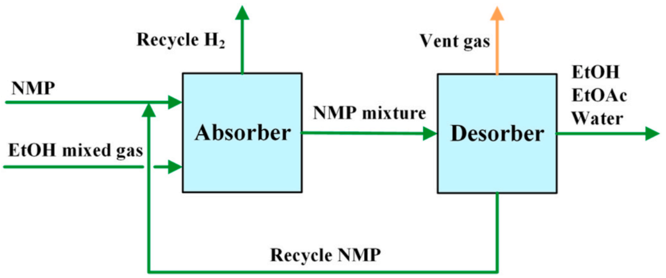

Fig. 10. Conceptual block flowsheet diagram of the crude separation process.

Investigating the effect of different variables on the recovery of ethanol and ethyl acetate in the absorber and the recovery of ethanol and NMP in the desorber improves ethanol recovery from the absorption process [44]. In the absorber, optimizable parameters are absorbent flow rate (F_a), the temperature of absorbent (T_a), the temperature of the gas (T_g), and the number of trays in the absorber (N_a). When optimum parameters of the absorber were reached, the pressure of the desorber (P_d), mole reflux ratio of the desorber (M_d), the feed position of the desorber (F_d), and the number of trays in the desorber (N_d) are varied to optimize the desorber. The initial parameters for steady state simulation of the absorption process are shown in Table 7.

3.2.2. Absorbent selection

A suitable absorbent is very important in the absorption process. The absorbent should be characterized by high solubility to ethanol, high T_b,

Table 7

Initial parameters for steady state simulation of the absorber and desorber.

Variables	Unit	Value
Absorbent flow rate	kg/h	2000
Temperature of absorbent	K	298.15
Temperature of the gas	K	298.15
Number of trays in the absorber		15
Pressure of the desorber	bar	0.4
Mole reflux ratio of the desorber		0.3
Feed position of the desorber		10
Number of trays in the desorber		20

low relative volatility, green, and not reacting with any components in the mixture [45]. In this work, NMP, EG, and Gly are analyzed and screened in terms of four aspects: T_b, saturated vapor pressure (P_{sv}), and ethanol and ethyl acetate recovery rate. The results are shown in Fig. 11.

As shown in Fig. 11a, the T_b of NMP is between EG and Gly and has a high T_b. From Fig. 11b, the P_{sv} of Gly at 298.15 K is very low. This indicates that the loss of Gly as absorbent is minimal. The P_{sv} of EG and NMP are larger than Gly but within reasonable limits. Fig. 11c, d represents the recovery of ethanol and ethyl acetate with different F_as to compare the solubility and selectivity of the absorbent to solute. It is obvious from Fig. 11c that all ethanol is recovered at a small NMP flow rate, which indicates that NMP has optimum ethanol solubility. Fig. 11d shows the recovery rates of ethyl acetate by different absorbents. EG and Gly have excellent recovery rates of ethanol. However, they are less able to absorb ethyl acetate. A relatively low NMP flow rate can efficiently reduce the energy consumption of the crude separation process. Therefore, NMP was used as a novel absorbent for ethanol to study the crude separation process.

3.2.3. *Optimum absorber parameters*

Fig. 12a–d gives the effect of different parameters on the recovery rates of ethanol and ethyl acetate in the absorber. Fig. 12a shows that by increasing F_a from 1000 kg/h to 6000 kg/h, ethanol has been fully recovered and the recovery rate of ethyl acetate dramatically increases. This indicates that NMP has excellent solubility and selectivity of ethanol. With F_a, greater than 3500 kg/h, the increasing trend of ethyl acetate recovery rate is no longer significant. If a larger F_a is used, it will increase absorbent losses. F_a of 3500 kg/h was selected to recover as much ethyl acetate as possible and increase the purity of recycled hydrogen. The F_a was optimized and the absorber recovered 99.99 % ethanol and 92.24 % ethyl acetate.

As shown in Fig. 12b, ethanol and ethyl acetate recovery rates are independent of T_a. The T_a of 298.15 K was chosen to avoid heating or cooling absorbent for economic efficiency and easy operation. At this point, ethanol and ethyl acetate recovery rates are 99.99 % and 92.27 %, respectively. As shown in Fig. 12c, the ethyl acetate recovery rate decreases with increasing T_g. Lower T_g significantly improves ethyl acetate recovery and reduces absorbent loss. Therefore, the T_g of 288.15 K was chosen to recover 99.99 % ethanol and 99.9 % ethyl acetate.

Based on the above optimization, ethanol and ethyl acetate recovery in the absorber has been at the optimum. We can reduce the equipment cost by appropriately reducing the N_a in the absorber. The effect of N_a on ethyl acetate recovery rate was shown in Fig. 12d–be insignificant for N_a greater than 10. The N_a of 10 was chosen and the ethanol and ethyl acetate recovery rates are 99.9 % and 99.5 %.

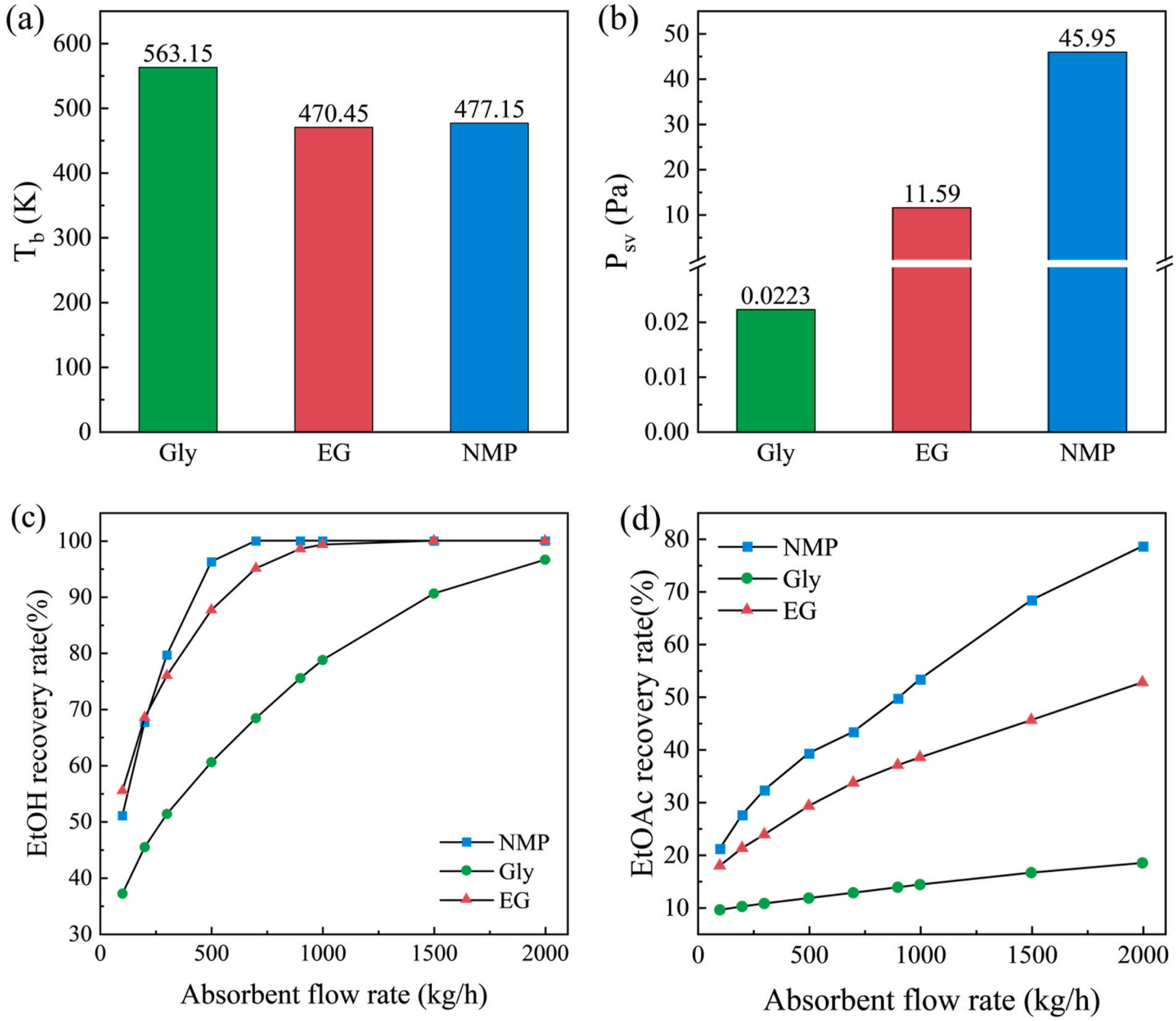

Fig. 11. (a) T_b of different absorbents at 298.15 K. (b) P_{sv} of different absorbents at 298.15 K. (c) EtOH recovery in the absorber by using different absorbents with varying flow rates. (d) EtOAc recovery in the absorber by using different absorbents with varying flow rates. Operating parameters in the absorber: T_a = 298.15 K, T_g = 298.15 K, N_a = 15.

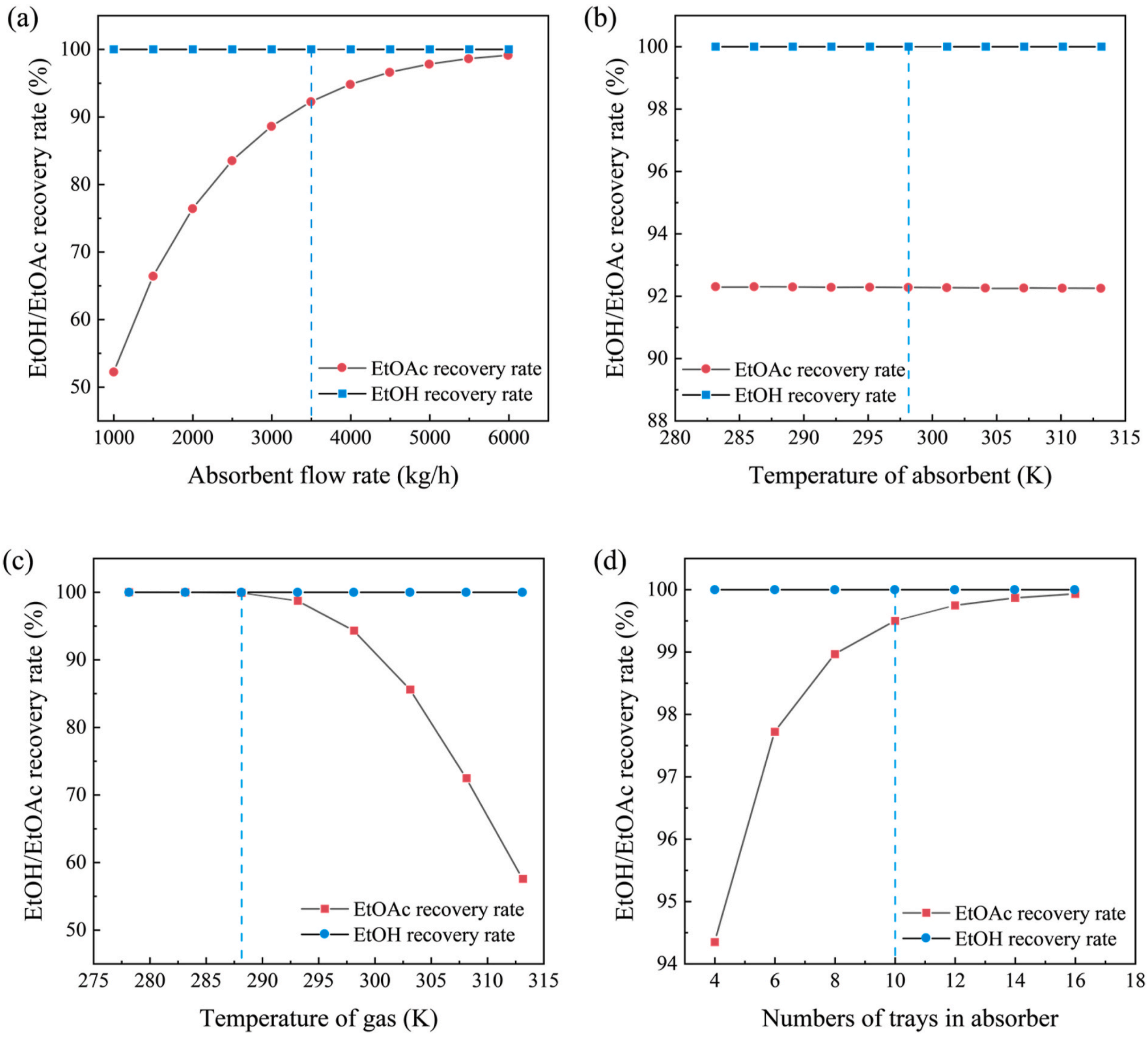

Fig. 12. (a) EtOH and EtOAc recovery rates with varying F_as. Operating parameters in the absorber: $T_a = 298.15$ K, $T_g = 298.15$ K, $N_a = 15$. (b) EtOH and EtOAc recovery rates with varying temperatures of absorbent. Operating parameters in the absorber: $F_a = 3500$ kg/h, $T_g = 298.15$ K, $N_a = 15$. (c) EtOH and EtOAc recovery rates with varying temperatures of the gas. Operating parameters in the absorber: $F_a = 3500$ kg/h, $T_a = 298.15$ K, $N_a = 15$. (d) EtOH and EtOAc recovery rates with varying numbers of trays in the absorber. Operating parameters in the absorber: $F_a = 3500$ kg/h, $T_a = 298.15$ K, $T_g = 288.15$ K.

3.2.4. Optimum desorber parameters

Fig. 13a–d represent the effect of P_d, M_d, F_d, and N_d on ethanol and NMP recovery in the desorber, respectively. From Fig. 13a, at a relatively low-pressure range, the ethanol recovery rate increases with increasing pressure, whereas the NMP recovery rate remains almost constant. The optimum P_d is 0.6 bar, at which the recovery of NMP and ethanol is 99.99 % and 98.86 %, respectively.

As shown in Fig. 13b, M_d does not affect NMP and ethanol recovery rates. This suggests that recovery of NMP is readily achievable and therefore reflux ratio of 0.3 was chosen to reduce the reboiler duty. In Fig. 13c, the effect of changing F_d on NMP and ethanol recovery rates has the same trend. When F_d is 5, the NMP and ethanol recovery rates are 99.99 % and 98.86 %, respectively. In Fig. 13d, the effect of changing N_d on NMP and ethanol recovery rates has the same trend. When N_d is greater than 8, ethanol and NMP recovery rates no longer vary. Therefore, less N_d is selected to reduce the equipment cost of the absorption process.

Once the operating parameters of the absorber and desorber have been optimized, the optimum absorption process modeling is achieved in Aspen Plus. Finally, the absorption process achieves 98 % ethanol recovery and 99.9 % NMP purity. In summary, the optimum parameters of the absorber and desorber are shown in Table 8.

3.3. Optimized reaction-crude separation process

The optimized reaction-crude separation (RCS) process is proposed based on the optimum design. Fig. 14 gives the process flow diagram of the RCS process. Fresh acetic acid is mixed with fresh hydrogen and recycled hydrogen that has passed through the compressor. The mixture passes through a heat exchanger and enters the ethanol synthesis reactor for reaction. After the reaction, the mixed gas containing hydrogen, ethanol, and ethyl acetate is heat-exchanged with the process stream inlet the reactor, which is then subjected to two-step condensing and separation. Step condensing not only separates most of ethanol but also saves energy. However, ethanol has not completely separated and hydrogen has not reached recycling purity. Then, ethanol mixed gas enters the absorber, and ethanol and ethyl acetate are removed by NMP. The recycled hydrogen continues participating in the reaction and NMP with ethanol enters the desorber. Finally, ethanol is separated and NMP is recycled back to the absorber. The total recovery rate of ethanol after two-step condensing and absorption is calculated at 99.98 %. The mixed ethanol containing mainly ethyl acetate, acetic acid, and water is

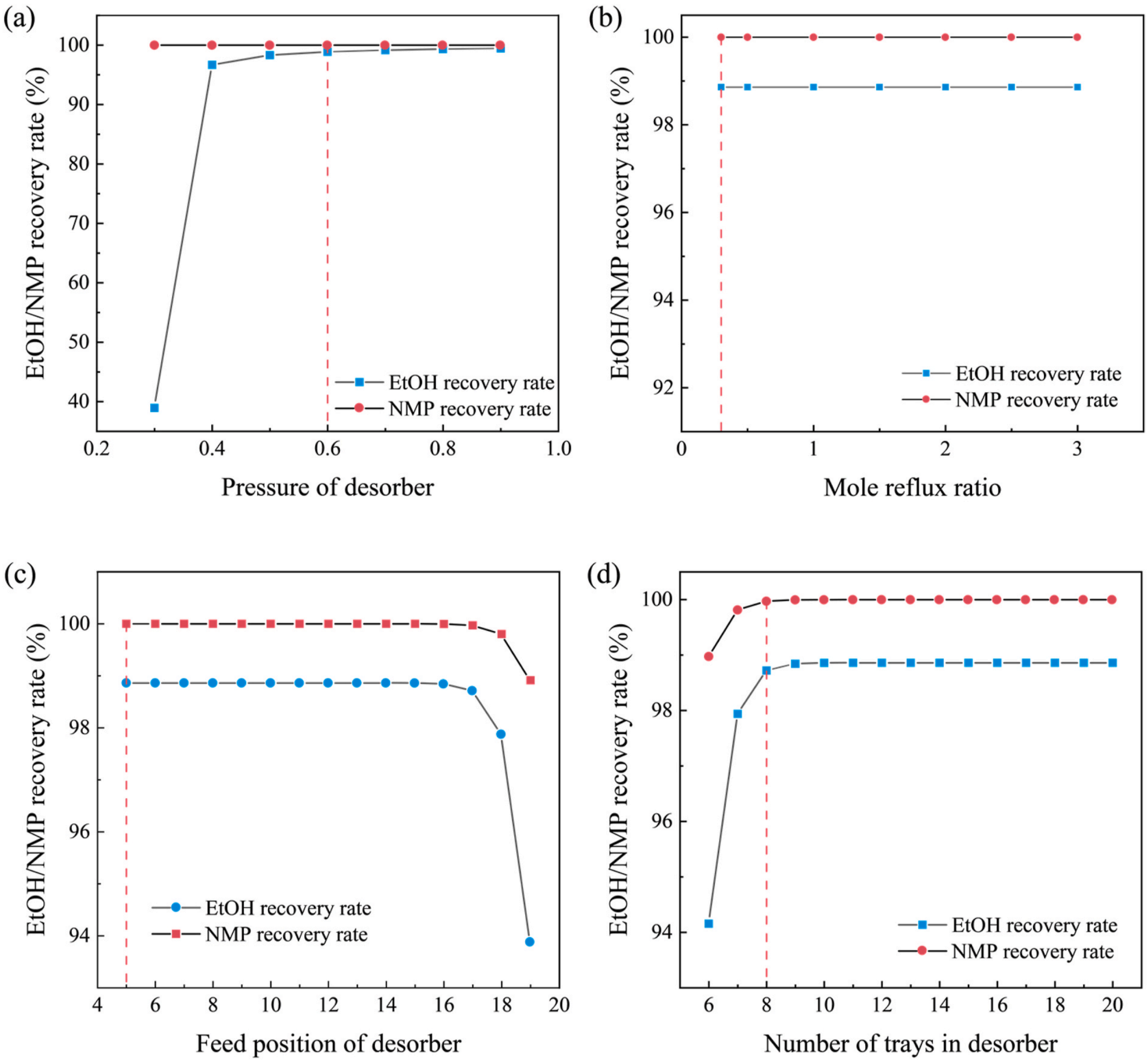

Fig. 13. (a) EtOH and NMP recovery rates with varying pressures of the desorber. Operating parameters in the desorber: $M_d = 0.3$, $F_d = 10$, $N_d = 20$. (b) EtOH and NMP recovery rates with varying mole reflux ratios. Operating parameters in the desorber: $P_d = 0.6$ bar, $F_d = 10$, $N_d = 20$. (c) EtOH and NMP recovery rates with varying feed positions of the desorber. Operating parameters in the desorber: $P_d = 0.6$ bar, $M_d = 0.3$, $N_d = 20$. (d) EtOH and NMP recovery rates with varying numbers of trays in the desorber. Operating parameters in the desorber: $P_d = 0.6$ bar, $M_d = 0.3$, $F_d = 5$.

Table 8
Optimum parameters of the absorber and desorber.

Variables	Unit	Value
Absorbent flow rate	kg/h	3500
Temperature of absorbent	K	298.15
Temperature of the gas	K	288.15
Number of trays in the absorber		10
Pressure of the desorber	bar	0.6
Mole reflux ratio of the desorber		0.3
Feed position of the desorber		5
Number of trays in the desorber		8

obtained from the RCS process.

In this work, the RCS process is divided into the ethanol reaction section and the crude separation section. The ethanol reaction section aims to realize efficient and safe production for ethanol with the multi-tubular fixed-bed reactor. The purpose of the crude separation section is to recover ethanol from the mixed gas by absorption, which realizes efficient separation of ethanol. No subsequent works on acetic acid-water and ethanol-ethyl acetate-water separation and purification are continued in this paper. Due to the maturity of the ethyl acetate synthesis process [46,47], some scholars have studied the separation of acetic acid-water [48,49] and ethanol-ethyl acetate-water systems [50,51], and these can be used as the reference and basis for the separation and purification of ethanol in this process.

4. Economic of optimized RCS process

Optimizing the process is not only important to achieve efficient production, but also to improve the economy [52]. The economy is regarded as one of the key bases for assessing project feasibility, so it is necessary to explore the economic process. Then, heat integration is proposed and used for energy saving and emissions reduction. In our work, the RCS process is evaluated and optimized in economic and environmental aspects to improve the competitiveness of acetic acid hydrogenation to ethanol in different routes for producing ethanol.

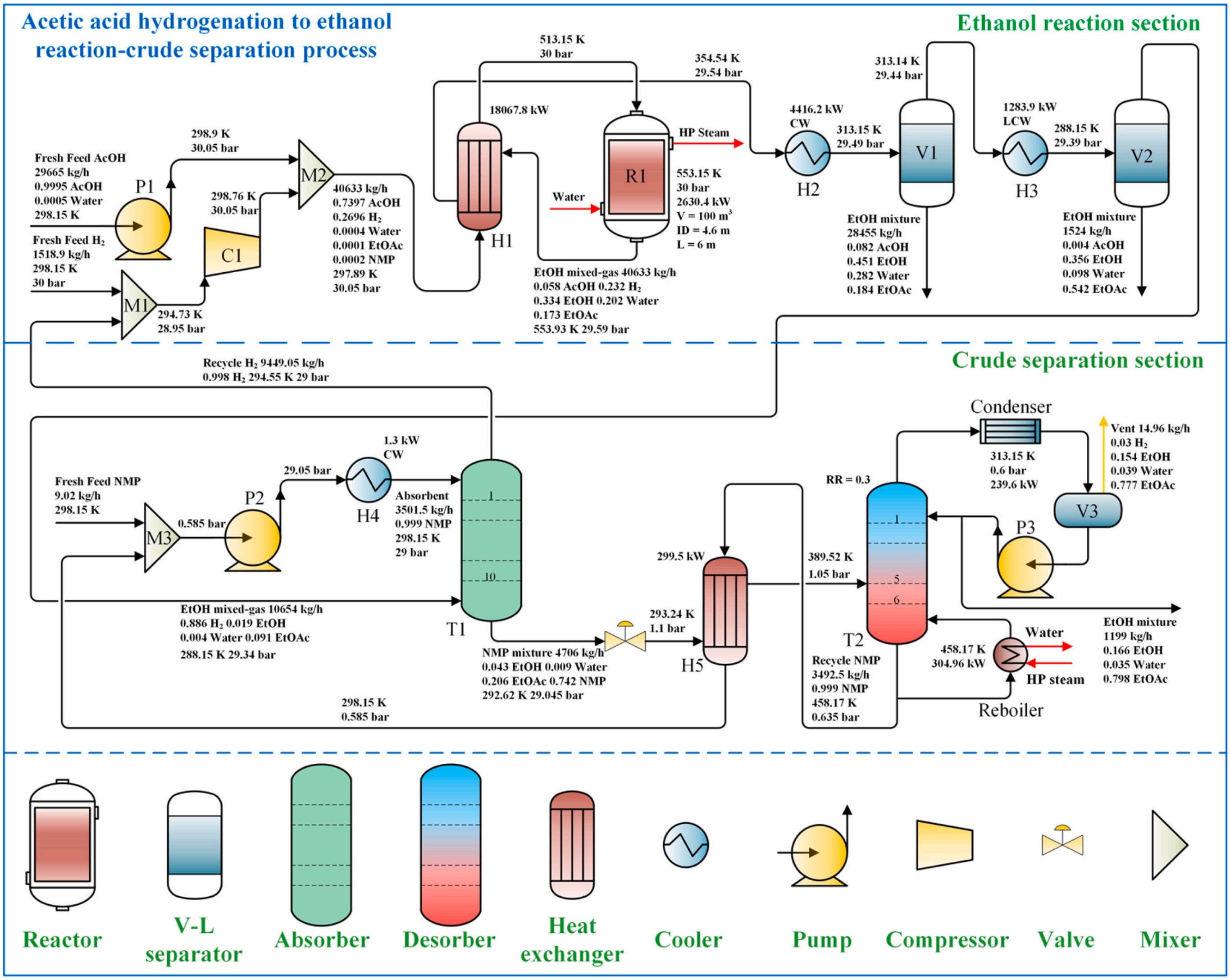

Fig. 14. Process flow diagram of acetic acid hydrogenation to ethanol reaction-crude separation process with optimized parameters.

4.1. Economic basis

In the overall chemical process design, we focus on the economic feasibility of the project. The total annual cost (TAC) proposed by Douglas [53]. as the evaluation criterion is used to assess chemical engineering designs.

$$\mathrm{TAC}(\times 10^6\$/\mathrm{year}) = \mathrm{OC} + \mathrm{CI}/\mathrm{PP} \tag{8}$$

PP represents the Payback Period, set at 3 years; OC denotes operating costs, including steam costs, electricity costs, and refrigerant water costs. Cooling water costs, significantly lower than steam costs, are neglected. The utility price can be referenced from Table S7 [54]. CI, namely capital investment, involves compressors, heat exchangers, reactors, vapor-liquid separators, columns, condensers, and reboilers. Small units such as pipes, valves, reflux tanks, and pumps are disregarded because of their relatively low cost. The diameters of the two columns are estimated using the “Tray Sizing” function in Aspen Plus, with a default tray spacing of 0.61 m. The overall tray efficiency for each column is assumed at 50 % for practice height design. Overall heat transfer coefficients for the condenser and reboiler are assumed at 0.852 kW/m^2/K and 0.568 kW/m^2/K respectively. Detailed calculation formulas related to CI can be found in Table S8 and the book [43].

4.2. Optimized RCS process

Table 9 provides the economic and CO_2 emissions of the optimized RCS process for synthesizing ethanol. CI is several times higher than OC, indicating that CI is the main cost for the RCS process. The TAC is 1.425 $\times$ 10^6 \$/year, and the cost of synthesizing ethanol with 100 ktpy is 14.25 \$/t. Although the RCS process does not include the separation and purification process, the cost per ton is still relatively appreciable.

CO_2 emissions are an important part of environmental protection evaluation [55]. Furnaces, gas turbines, and boilers are major contributors to CO_2 emissions. These utility devices are the energy consumers in the refining plants and are used to provide heat, steam, and power to the process by burning fuel [56]. Hence, CO_2 emissions should also draw our attention. Relevant formulas and calculation methods are derived from Gadalla [56], Yang [57], and Shen [55], as follows:

Table 9
Economic and CO_2 emissions for optimized RCS process.

Parameters	Value
OC ($\times$ 10^6 \$/year)	0.425
CI ($\times$ 10^6 \$)	3.001
TAC ($\times$ 10^6 \$/year)	1.425
CO_2 emissions ($\times$ 10^2 kg/h)	1.230

$$\text{Carbon dioxide Emissions} = (\text{Qfuel} / \text{NHV})(\text{C\%} / 100)\alpha \tag{9}$$

Qfuel (kJ/h) is the total heat of the heating device and the total power of the compressor and pump in the OP and HIR process. α is 3.67 in the equation, and the NHV (kJ/kg) represents the net heating value of a fuel containing a carbon content of C %. The calculation formula for Qfuel and additional detailed parameters are available in Table S9. The CO_2 emissions are 1.23×10^2 kg/h from Table 9.

Table 10
Economic and CO_2 emissions for optimized RCS process with heat integration.

Parameters	Value
OC ($\times 10^6$ \$/year)	0.270
CI ($\times 10^6$ \$)	3.001
TAC ($\times 10^6$ \$/year)	1.270
CO_2 emissions ($\times 10^2$ kg/h)	0.516

4.3. *Optimized RCS process with heat integration*

Heat integration offers great potential to reduce energy costs and carbon emissions in plants [55]. Since the reactor can by-produce high-pressure steam, heuristic heat integration can be used to improve the efficiency of heat utilization in the system. Therefore, the optimized RCS process with heat integration (RCS-HI) has been proposed to compare their energy saving, economic, and environmental aspects with the optimized RCS process.

High-pressure steam generated from the reactor is used to heat the desorber which is heuristic heat integration in Fig. 15 Economic and CO_2 emissions of the RCS-HI process are represented in Table 10 and it indicates that there is a significant reduction in economic and CO_2 emissions with heat integration. In addition, since the main energy consumption in acetic acid hydrogenation to ethanol is concentrated in the separation and purification process [58], the excess high-pressure steam can energize it which will substantially increase heat utilization of the plant and then further reduce the cost of production.

Based on the above-completed work, a quantitative comparison between the RCS process and the RCS-HI process is investigated in terms of the economic and CO_2 emissions, as provided in Fig. 16. The key benefit of heat integration is saving OC. The reduction rate is the difference between the RCS process and the RCS-HI process of OC, TAC, and CO_2 emissions divided by the value of the RCS process. It is revealed that the RCS-HI process offers a significant reduction in OC and TAC by 36.5 % and 10.9 %, respectively, compared with the RCS process. Then, we also found that the RCS-HI process offers considerable CO_2 emissions reduction by 58.1 % compared with the RCS process, as in Fig. 16. In summary, the RCS-HI process has significant advantages over the RCS

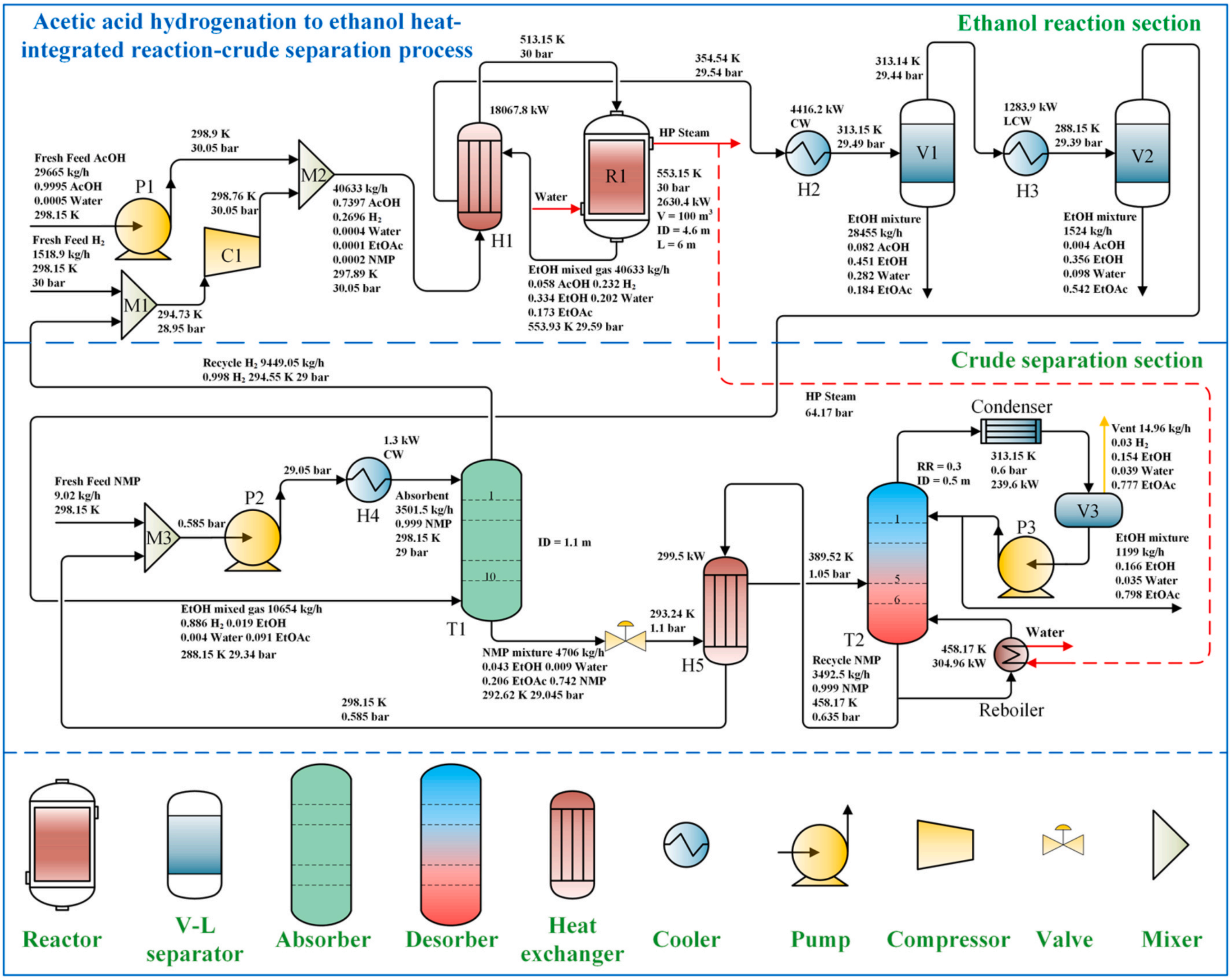

Fig. 15. Process flow diagram of optimized reaction-crude separation process with heat integration.

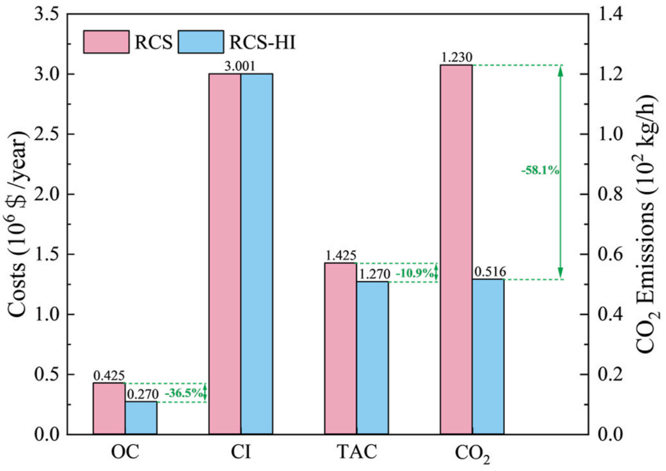

Fig. 16. Comparison of costs and CO_2 emissions between the RCS and RCS-HI processes.[a]

[a] Reduction rate = ($Item_{RCS\text{-}HI}$- $Item_{RCS}$)/$Item_{RCS}$ × 100 %, Item = OC, TAC, CO_2 emissions.

process for acetic acid hydrogenation to ethanol.

5. Conclusions

To address a high-efficiency, energy-saving, low-carbon reaction of acetic acid hydrogenation to ethanol, we explore the reaction-crude separation process with heat integration, which shows significant economic and CO_2 emissions advantages. A coupled design approach that combines kinetics with transfers is proposed to design and optimize the multi-tubular fixed-bed reactor. Rigorous design and global optimization of structural and operating parameters make reaction performance optimum and reasonable by the proposed approach. Thereafter, we explore a crude separation process including absorption and desorption to recover all ethanol based on the NRTL-HOC model with regressed binary interaction parameters, NMP is selected as the most suitable absorbent. The optimized crude separation process shows that ethanol can be recovered with 98 %. Furthermore, we compare the optimized reaction-crude separation process to the process with heat integration from heuristics. The results revealed that the heat-integrated process has significant economic and low-carbon advantages with reductions of 36.5 % in OC, 10.9 % in TAC, and 58.1 % in CO_2 emissions. This work could provide a feasible and promising reactor and crude separation process for acetic acid hydrogenation to ethanol, which features economic, high-efficient, energy-saving, and low-carbon. Further study should consider that catalyst particle size has an impact on efficiency of particles and investigate purification and separation for ethanol, which can be quite beneficial to the application of the research results.

CRediT authorship contribution statement

Can Zhou: Writing – review & editing, Writing – original draft, Visualization, Methodology, Investigation, Formal analysis, Conceptualization. **Chen-Xi You:** Writing – review & editing, Writing – original draft, Software. **Yang Liu:** Writing – review & editing, Writing – original draft, Software. **Hui Shi:** Writing – review & editing, Validation, Resources, Investigation, Funding acquisition. **Chengtian Cui:** Writing – review & editing, Validation, Resources. **Jihai Tang:** Writing – review & editing, Resources, Funding acquisition. **Mifen Cui:** Writing – review & editing, Resources, Funding acquisition. **Xu Qiao:** Writing – review & editing, Resources, Funding acquisition. **Ming Xia:** Writing – review & editing, Writing – original draft, Validation, Supervision, Software, Resources, Project administration, Methodology, Funding acquisition, Conceptualization.

Declaration of competing interest

Acknowledgments

This work was financially supported by the Natural Science Foundation of China (Grant No. 22202225, 22208361, 22208154), and New Talent Start-up Fund Project of Nanjing Tech University (Grant No. 39801177).

Nomenclature

Item		Item	
EtOH	ethanol	u_m	superficial gas velocity
AcOH	acetic acid	ε_b	bed voidage
NMP	n-methyl-2-pyrrolidone	d_s	catalyst particle size
STY	space-time yield	Re_M	corrected Reynolds number
M_{cat}	catalyst loading	μ	gas viscosity
ΔP	pressure drop	d_i	inner diameter of the tube
EG	ethylene glycol	T_s	temperature of saturated water
Gly	glycerol	P_p	pressure of the process stream
EtOAc	ethyl acetate	M_r	mole ratio of hydrogen to acetic acid
LHHW	Langmuir-Hinshelwood-Hougen-Watson	T_p	temperature of the process stream
WHSV	weight hourly space velocity	F_a	absorbent flow rate
H_2	hydrogen	T_a	temperature of absorbent
VLE	vapor-liquid equilibrium	T_g	temperature of the gas
V_b	volume of the bed	N_a	number of trays in the absorber
V_r	volume of the reactor	P_d	pressure of the desorber
L	bed height	M_d	mole reflux ratio of the desorber
N_t	number of tubes	F_d	feed position of the desorber
U	overall heat-transfer coefficient	N_d	number of trays in the desorber
α_b	convective heat-transfer coefficient from the bed to the tube wall	T_b	bubble point
α_f	convective heat-transfer coefficient of saturated water outside the tube to the tube wall	P_{sv}	saturated vapor pressure
λ_s	thermal conductivity of the tube wall	TAC	total annual cost
δ	tube wall thickness	OC	operating cost
R_c	fouling coefficient of the bed and outside of the tube	CI	capital investment
f'	coefficient of frictional resistance	RCS	reaction-crude separation
P	density of the gas	RCS-HI	reaction-crude separation with heat-integration

Appendix A. Supplementary data

Supplementary data to this article can be found online at https://doi.org/10.1016/j.ijhydene.2025.04.209.

References

[1] Liu J, Zhang Z, Sun M, Kong J, Dong M, Sun L. Intensification and performance assessment of ethanol production process by hydrogenation of methyl acetate. Chem Eng Res Des 2023;189:619–35. https://doi.org/10.1016/j.cherd.2022.11.023.

[2] Dong X, Lei J, Chen Y, Jiang H, Zhang M. Selective hydrogenation of acetic acid to ethanol on Cu-In catalyst supported by SBA-15. Appl Catal, B 2019;244:448–58. https://doi.org/10.1016/j.apcatb.2018.11.062.

[3] He L, Zhou B-C, Sun D-H, Li W-C, Lv W-L, Wang J, et al. Catalytic conversion of ethanol to oxygen-containing value-added chemicals. ACS Catal 2023;13:11291–304. https://doi.org/10.1021/acscatal.3c01481.

[4] Latif MN, Wan Isahak WNR, Samsuri A, Hasan SZ, Manan WN, Yaakob Z. Recent advances in the technologies and catalytic processes of ethanol production. Catalysts 2023;13. https://doi.org/10.3390/catal13071093.

[5] Sunley GJ, Watson DJ. High productivity methanol carbonylation catalysis using iridium: the Cativa™ process for the manufacture of acetic acid. Catal Today 2000;58:293–307. https://doi.org/10.1016/S0920-5861(00)00263-7.

[6] Yoneda N, Kusano S, Yasui M, Pujado P, Wilcher S. Recent advances in processes and catalysts for the production of acetic acid. Appl Catal, A 2001;221:253–65. https://doi.org/10.1016/S0926-860X(01)00800-6.

[7] Zhang S, Duan X, Ye L, Lin H, Xie Z, Yuan Y. Production of ethanol by gas phase hydrogenation of acetic acid over carbon nanotube-supported Pt–Sn nanoparticles. Catal Today 2013;215:260–6. https://doi.org/10.1016/j.cattod.2013.05.002.

[8] Pan D, Zhou J, Peng B, Wang S, Zhao Y, Ma X. The cooperation effect of Ni and Pt in the hydrogenation of acetic acid. Front Chem Sci Eng 2021;16:397–407. https://doi.org/10.1007/s11705-021-2076-4.

[9] Pallassana V, Neurock M. Reaction paths in the hydrogenolysis of acetic acid to ethanol over Pd(111), Re(0001), and PdRe alloys. J Catal 2002;209:289–305. https://doi.org/10.1006/jcat.2002.3585.

[10] Ito Y, Kawamoto H, Saka S. Efficient and selective hydrogenation of aqueous acetic acid on Ru–Sn/TiO_2 for bioethanol production from lignocellulosics. Fuel 2016;178:118–23. https://doi.org/10.1016/j.fuel.2016.03.043.

[11] Chen L, Zhu Y, Zheng H, Zhang C, Zhang B, Li Y. Aqueous-phase hydrodeoxygenation of carboxylic acids to alcohols or alkanes over supported Ru catalysts. J Mol Catal Chem 2011;351:217–27. https://doi.org/10.1016/j.molcata.2011.10.015.

[12] Zhou M, Zhang H, Ma H, Ying W. Insight on mechanism of Sn modification in alumina supported RhSn catalysts for acetic acid hydrogenation to fuel-grade ethanol. Fuel 2017;203:774–80. https://doi.org/10.1016/j.fuel.2017.03.063.

[13] Shi H, Xia M, Lu H, Xie Q, Jia L, Hou B, et al. Theoretical investigation of the reactivity of flat Ni (111) and stepped Ni (211) surfaces for acetic acid hydrogenation to ethanol. Int J Hydrogen Energy 2021;46:15454–70. https://doi.org/10.1016/j.ijhydene.2021.02.045.

[14] Zhang M, Yao R, Jiang H, Li G, Chen Y. Insights into the mechanism of acetic acid hydrogenation to ethanol on Cu(111) surface. Appl Surf Sci 2017;412:342–9. https://doi.org/10.1016/j.apsusc.2017.03.222.

[15] Chen Y, Zhai Z, Liu J, Zhang J, Geng Z, Lyu H. The synergistic effects of Cu clusters and In_2O_3 on ethanol synthesis from acetic acid hydrogenation. Phys Chem Chem Phys 2019;21:23906–15. https://doi.org/10.1039/c9cp04766b.

[16] Chen Q, Zhang X, Tian S, Long J, Meng X, Sun Q, et al. Kinetics of hydrogenation of acetic acid to ethanol. Asian J Chem 2019;31:2915–23. https://doi.org/10.14233/ajchem.2019.22277.

[17] Zhang M, Du J, Chen Y. Hydrodeoxygenation of acetic acid over Ni-promoted Cu-based catalysts: a theoretical mechanism and kinetic study. Catal Sci Technol 2023;13:1345–57. https://doi.org/10.1039/d2cy02097a.

[18] Lawal AM, Hart A, Daly H, Hardacre C, Wood J. Kinetics of hydrogenation of acetic acid over supported platinum catalyst. Energy Fuel 2019;33:5551–60. https://doi.org/10.1021/acs.energyfuels.9b01062.

[19] Zhou M, Zhang H, Ma H, Ying W. The catalytic properties of K modified PtSn/Al_2O_3 catalyst for acetic acid hydrogenation to ethanol. Fuel Process Technol 2016;144:115–23. https://doi.org/10.1016/j.fuproc.2015.12.022.

[20] Chang W, Wan H, Guan G, Yao H. Isobaric vapor–liquid equilibria for water+acetic acid+(N-methyl pyrrolidone or N-methyl acetamide). Fluid Phase Equilib 2006;242:204–9. https://doi.org/10.1016/j.fluid.2006.02.002.

[21] Yang J, Pan X, Yu M, Cui P, Ma Y, Wang Y, et al. Vapor–liquid equilibrium for binary and ternary systems of tetrahydrofuran, ethyl acetate and N-methyl pyrrolidone at pressure 101.3 kPa. J Mol Liq 2018;268:19–25. https://doi.org/10.1016/j.molliq.2018.07.038.

[22] Amin M, Butt AS, Ahmad J, Lee C, Azam SU, Mannan HA, et al. Issues and challenges in hydrogen separation technologies. Energy Rep 2023;9:894–911. https://doi.org/10.1016/j.egyr.2022.12.014.

[23] Silva RJMCL, Souza TPC, Elihimas DRM, Silva JP, Albuquerque AA, Pacheco JGA, et al. Ethanol dehydration by absorption and biodiesel production by reactive distillation: an innovative integrated process. Biomass Bioenergy 2021;154. https://doi.org/10.1016/j.biombioe.2021.106263.

[24] Cardoso VM, Bernardo A, Giulietti M. Ethanol absorption from CO_2 using solutions of glycerol and glycols. Chem Eng Commun 2018;205:1507–19. https://doi.org/10.1080/00986445.2018.1458027.

[25] Zhou M, Zhang H, Ma H, Ying W. Kinetic modeling of acetic acid hydrogenation to ethanol over K-modified PtSn catalyst supported on alumina. Ind Eng Chem Res 2017;56:8833–42. https://doi.org/10.1021/acs.iecr.7b01859.

[26] Luyben WL. Design and control of a methanol reactor/column process. Ind Eng Chem Res 2010;49:6150–63. https://doi.org/10.1021/ie100323d.

[27] Chen W-L, Hsu C-C, Lin S-T. Prediction of phase behaviors of acetic acid containing fluids. Fluid Phase Equilib 2013;353:61–8. https://doi.org/10.1016/j.fluid.2013.05.039.

[28] Zhu D, Gao D, Zhang H, Winter B, Lücking P, Sun H, et al. Geometric structures of associating component optimized toward correlation and prediction of isobaric vapor–liquid equilibria for binary and ternary mixtures of ethanal, ethanol, and ethanoic acid. J Chem Eng Data 2012;58:7–17. https://doi.org/10.1021/je300810p.

[29] Xin H, Wang XF, Li JQS. Isobaric vapor-liquid equilibria for the system containing acetic acid at 101.3kPa. Adv Mater Res 2012;560–561:79–85. https://doi.org/10.4028/www.scientific.net/AMR.560-561.79.

[30] Hayden JG, O'Connell JP. A generalized method for predicting second virial coefficients. Ind Eng Chem Process Des Dev 1975;14:209–16. https://doi.org/10.1021/i260055a003.

[31] Nurjanah I, Hsieh L-HC, Chiang Y-H, Sean W-Y. Energy saving in NMP (N-methyl-2-pyrrolidone) recovery process by numerical modeling. Environ Technol Innov 2023;31. https://doi.org/10.1016/j.eti.2023.103218.

[32] Rakshit PK, Pathak S, Voolapalli RK, Upadhyayula S. Thermodynamic analysis, kinetics modeling, and reactor model development for acetic acid hydrogenation reaction over bimetallic Pt–Sn catalyst. Energy Fuel 2020;34:3640–8. https://doi.org/10.1021/acs.energyfuels.9b04070.

[33] Ermolaev VS, Gryaznov KO, Mitberg EB, Mordkovich VZ, Tretyakov VF. Laboratory and pilot plant fixed-bed reactors for Fischer–Tropsch synthesis: mathematical modeling and experimental investigation. Chem Eng Sci 2015;138:1–8. https://doi.org/10.1016/j.ces.2015.07.036.

[34] Rinaldi R, Visconti CG. Flexible operations of a multi-tubular reactor for methanol synthesis from biogas exploiting green hydrogen. Chem Eng Sci 2023;272. https://doi.org/10.1016/j.ces.2023.118611.

[35] Couto CS, Madeira LM, Nunes CP, Araújo P. Liquid-phase hydrogenation of nitrobenzene in a tubular reactor: parametric study of the operating conditions influence. Ind Eng Chem Res 2017;56:3231–42. https://doi.org/10.1021/acs.iecr.7b00403.

[36] Huang H, Cao C, Wang Y, Yang Y, Lv J, Xu J. Model-based analysis for ethylene carbonate hydrogenation operation in industrial-type tubular reactors. Processes 2022;10. https://doi.org/10.3390/pr10040688.

[37] Jess A, Kern C. Modeling of multi-tubular reactors for fischer-tropsch synthesis. Chem Eng Technol 2009;32:1164–75. https://doi.org/10.1002/ceat.200900131.

[38] Wei R, Yan C, Yang A, Shen W, Li J. Improved process design and optimization of 200 kt/a ethylene glycol production using coal-based syngas. Chem Eng Res Des 2018;132:551–63. https://doi.org/10.1016/j.cherd.2018.02.006.

[39] Alipour-Dehkordi A, Khademi MH. Use of a micro-porous membrane multi-tubular fixed-bed reactor for tri-reforming of methane to syngas: CO_2, H_2O or O_2 side-feeding. Int J Hydrogen Energy 2019;44:32066–79. https://doi.org/10.1016/j.ijhydene.2019.10.097.

[40] Darvishi A, Davand R, Khorasheh F, Fattahi M. Modeling-based optimization of a fixed-bed industrial reactor for oxidative dehydrogenation of propane. Chin J Chem Eng 2016;24:612–22. https://doi.org/10.1016/j.cjche.2015.12.018.

[41] Ergun S. Fluid flow through packed columns. J Mater Sci Chem Eng 1952;48:89–94.

[42] Pan J, Ding Y, Li J, Xie L, Xu Z, Wu H, et al. Economic, entropy generation and environmental analysis of separation of high-concentration azeotropic mixtures by an innovative extractive distillation configuration based on multi-objective optimization. Sep Purif Technol 2024;340. https://doi.org/10.1016/j.seppur.2024.126729.

[43] Luyben WL. Principles and case studies of simultaneous design. first ed. Hoboken: John Wiley & Sons; 2011.

[44] Law LC, Yusoff Azudin N. Abd. Shukor SR. Optimization and economic analysis of amine-based acid gas capture unit using monoethanolamine/methyl diethanolamine. Clean Technol Environ Policy 2017;20:451–61. https://doi.org/10.1007/s10098-017-1430-1.

[45] Lu M, Zhao X, Zhou J, Qian G, Duan X, Yuan W, et al. Solvent screening and process optimization for separating propylene oxide from direct propylene epoxidation with H_2 and O_2. Ind Eng Chem Res 2018;58:395–402. https://doi.org/10.1021/acs.iecr.8b05407.

[46] Chien IL, Teng Y-P, Huang H-P, Tang YT. Design and control of an ethyl acetate process: coupled reactor/column configuration. J Process Control 2005;15:435–49. https://doi.org/10.1016/j.jprocont.2004.07.003.

[47] Lee H-Y, Huang H-P, Chien IL. Control of reactive distillation process for production of ethyl acetate. J Process Control 2007;17:363–77. https://doi.org/10.1016/j.jprocont.2006.10.002.

[48] Jullok N, Luis P, Degrève J, Van der Bruggen B. A cascaded pervaporation process for dehydration of acetic acid. Chem Eng Sci 2014;105:208–12. https://doi.org/10.1016/j.ces.2013.11.011.

[49] Chien IL, Zeng K-L, Chao H-Y, Hong Liu J. Design and control of acetic acid dehydration system via heterogeneous azeotropic distillation. Chem Eng Sci 2004;59:4547–67. https://doi.org/10.1016/j.ces.2004.06.041.

[50] Cheng H, Zhong J, Dai Y, Jiao Y, Zhu Z, Cui P, et al. Design and multiple performance evaluation of green energy saving process for ethyl acetate/ethanol/water azeotrope separation by extractive distillation based on mixed solvent. J Clean Prod 2023;421. https://doi.org/10.1016/j.jclepro.2023.138565.

[51] Ma S, Shang X, Li L, Song Y, Pan Q, Sun L. Energy-saving thermally coupled ternary extractive distillation process using ionic liquids as entrainer for separating ethyl acetate-ethanol-water ternary mixture. Sep Purif Technol 2019;226:337–49. https://doi.org/10.1016/j.seppur.2019.05.103.

[52] Hu R, Liu W, Wang Y, Zhu Z, Wang Y, Yang J, et al. Mechanism analysis and process optimization for extraction distillation of alcohol-ester azeotrope using ionic liquid. ACS Sustainable Chem Eng 2024;12:16770–80. https://doi.org/10.1021/acssuschemeng.4c07089.

[53] Pham HN, Doherty MF. Design and synthesis of heterogeneous azeotropic distillations—II. Residue curve maps. Chem Eng Sci 1990;45:1837–43. https://doi.org/10.1016/0009-2509(90)87059-2.

[54] Turton R, Bailie RC, Whiting WB, Shaeiwitz JA. Analysis, synthesis and design of chemical processes. third ed. New York: Prentice Hall; 2009.

[55] Shi T, Chun W, Yang A, Su Y, Jin S, Ren J, et al. Optimization and control of energy saving side-stream extractive distillation with heat integration for separating ethyl acetate-ethanol azeotrope. Chem Eng Sci 2020;215. https://doi.org/10.1016/j.ces.2019.115373.

[56] Gadalla MA, Olujic Z, Jansens PJ, Jobson M, Smith R. Reducing CO_2 emissions and energy consumption of heat-Integrated distillation systems. Environ Sci Technol 2005;39:6860–70. https://doi.org/10.1021/es049795q.

[57] Yang A, Sun S, Eslamimanesh A, Wei Sa, Shen W. Energy-saving investigation for diethyl carbonate synthesis through the reactive dividing wall column combining the vapor recompression heat pump or different pressure thermally coupled technique. Energy 2019;172:320–32. https://doi.org/10.1016/j.energy.2019.01.126.

[58] Meng D, Dai Y, Xu Y, Wu Y, Cui P, Zhu Z, et al. Energy, economic and environmental evaluations for the separation of ethyl acetate/ethanol/water mixture via distillation and pervaporation unit. Process Saf Environ Prot 2020;140:14–25. https://doi.org/10.1016/j.psep.2020.04.039.